



저작자표시-비영리-변경금지 2.0 대한민국

이용자는 아래의 조건을 따르는 경우에 한하여 자유롭게

- 이 저작물을 복제, 배포, 전송, 전시, 공연 및 방송할 수 있습니다.

다음과 같은 조건을 따라야 합니다:



저작자표시. 귀하는 원저작자를 표시하여야 합니다.



비영리. 귀하는 이 저작물을 영리 목적으로 이용할 수 없습니다.



변경금지. 귀하는 이 저작물을 개작, 변형 또는 가공할 수 없습니다.

- 귀하는, 이 저작물의 재이용이나 배포의 경우, 이 저작물에 적용된 이용허락조건을 명확하게 나타내어야 합니다.
- 저작권자로부터 별도의 허가를 받으면 이러한 조건들은 적용되지 않습니다.

저작권법에 따른 이용자의 권리는 위의 내용에 의하여 영향을 받지 않습니다.

이것은 [이용허락규약\(Legal Code\)](#)을 이해하기 쉽게 요약한 것입니다.

[Disclaimer](#)

Master's Thesis

A bi-polymer-crosslinked binder to improve the kinetics of sodiation, desodiation and reversibility of antimony for sodium ion battery anodes.

Dohyoung Kim

Department of Chemical Engineering

Graduate School of UNIST

2019

A bi-polymer-crosslinked binder to improve the kinetics of sodiation, desodiation and reversibility of antimony for sodium ion battery anodes.

Dohyoung Kim

Department of Chemical Engineering

Graduate School of UNIST

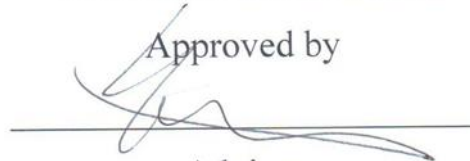
A bi-polymer-crosslinked binder to improve the  
kinetics of sodiation, desodiation and reversibility  
of antimony for sodium ion battery anodes.

A thesis  
submitted to the Graduate School of UNIST  
in partial fulfillment of the  
requirements for the degree of  
Master of Science

Dohyoung Kim

05/27/2019 of submission

Approved by



Advisor

Hyun-Kon Song

A bi-polymer-crosslinked binder to improve the kinetics of sodiation, desodiation and reversibility of antimony for sodium ion battery anodes.

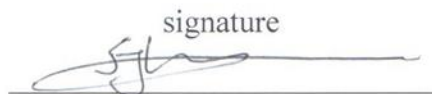
Dohyoung Kim

This certifies that the thesis of Dohyoung Kim is approved.

05/27/2019 of submission

signature  


Advisor: Hyun-Kon Song

signature  


Seok Ju Kang: Thesis Committee Member #1

signature  


Nam-Soon Choi: Thesis Committee Member #2

three signatures total in case of masters



## Abstract

Antimony has been developed as a promising anode material of sodium ion batteries (SIBs) even if its volume is tremendously expanded during the alloying reaction with sodium. Repeated volume changes along sodiation/desodiation cycles encourage capacity fading by triggering pulverization accompanying electrolyte decomposition. Also, low cation transference number of sodium ion is another huddle of SIBs. In this work, a binder for antimony in SIB cells was designed to have bifunctionality to improve (1) the mechanical toughness to suppress the serious volume change and (2) the transference number of sodium ion. A crosslinked composite of poly(acrylic acid) (PAA) and cyanoethyl pullulan (pullulan-CN) was presented as the binder. The polysaccharide backbone of pullulan-CN was responsible for the mechanical toughness while the cyanoethyl groups improved by pullulan-CN. The antimony-based SIB cells using the composite binder showed improved cycle life with enhanced kinetics.

**KEYWORDS** : Na-ion batteries, antimony, polysaccharide binder, cross-linked binder, cation migration





**Contents**  
**Abstract**  
**List of figures**  
**List of tables**  
**List of schemes**  
**Nomenclature**

**Chapter 1. Introduction**

1.1 Importance of secondary batteries in the future -----	1
1.2 Introduction of alloy anode materials for lithium ion batteries (LIBs) -----	2
1.2.1 Recent studies for binders to improve alloy anode materials in LIB system---	3
1.3 Comparison of LIB and sodium ion batteries (SIBs) -----	7
1.4 Introduction of anode materials for SIBs-----	8
1.4.1 Recent studies for binders to improve alloy anode materials in SIB system ---	9
1.4.2 Other problems of SIBs anode and strategies to solve this problem-----	10

**Chapter 2. A crosslinked binder to enhance the performance of antimony anode for sodium-ion batteries**

2.1 Introduction -----	12
2.2 Experimental method and materials-----	12
2.2.1 Binder & Antimony preparation-----	12
2.2.2 Cell preparation-----	13
2.2.3 Mechanical characterization-----	14
2.2.4 Electrochemical characterization-----	14
2.2.5 Material characterization-----	15
2.3 Results and discussion -----	15
2.4 Conclusion -----	27
2.5 Reference -----	28

## List of Figures

**Figure 1.** List of rechargeable batteries comparing with volumetric and gravimetric energy density. <sup>1</sup>

**Figure 2.** The number of Lithium demand, availability, electric vehicles (EVs), hybrid electric vehicles (HEVs) and plugin hybrid electric vehicles (PHEVs) over time. According to the availability of lithium and demand of EV/HEV/PHEV, run out of lithium the near future could be occurred. <sup>2</sup>

**Figure 3.** Polysaccharides polymeric binders characterized by glycosidic linkages between their monomeric units and functional moieties on side chains. (a) Molecular structures of polysaccharides: CMC, pectin. (b) Schematic figure of morphological changes of two polysaccharides binders and silicon particles along lithiation and delithiation: white strands = polymeric binders; red points = covalent bonds between hydroxyl and carboxylate moieties of binder; blue points = condensation reaction of between carboxylate of binders and hydroxyl moieties of silicon oxide films on the silicon particles <sup>3</sup>

**Figure 4.** (a) Structure of alginate, CMC and pullulan. Glycosidic linkage ( $\alpha$ ,  $\beta$ ) of each polymeric binder were indicated. (b) Covalent condensation between surface oxide of Si and carboxylate of PAA as well as between pullulan and PAA after thermal heating at 150 °C. Dehydration reactions are induced at 150 °C between carboxylic moieties of PAA and hydroxyl moieties of pullulan and surface oxide of silicon. (c) FT-IR spectra of PAA, pullulan and PAA/pullulan, confirming the cross-linking of two binders by disappearance of hydroxyl moiety and appearance of ester moiety <sup>4</sup>

**Figure 5.** Natural abundance in the crust of earth. <sup>5</sup>

**Figure 6.** (upper) Initial charge and discharge profiles and (bottom) cyclability of (a) hard-carbon with PVdF binder, (b) Sn-PAA, (c) Pb-PAA, (d) Si-PAA, and (e) Sn-PVdF. The hard-carbon electrodes were characterized in beaker-type Na cells at 25 mA g<sup>-1</sup>, and Sn, Pb, Si and Sn based electrodes were tested in coin-type cells at 50 mA g<sup>-1</sup> in 1.0 M NaClO<sub>4</sub> PC. <sup>6</sup>

**Figure 7.** Electrochemical performance of PAA/PVA-CN or PAA/CMC binder-based silicon anodes. Cyclability and coulombic efficiency along continuous cycles of lithiation and delithiation at 25 °C (a) and 60 °C. (b) Rate performance of silicon anodes. Controlling delithiation of silicon anodes with lithiation fixed at 0.2 C (c) Same lithiation/delithiation C-rate were used for (d). Cyclability at 1 C/1 C cycles. (e) <sup>7</sup>

**Figure 8.** Structural informations about three polymers and their cross-linked bipoymers. The disappearance of hydroxyl and carboxylate moieties in the crosslinked polymers, appearance of ester moieties of cross-linked bi-polymer binders and remained nitrile groups measured by FT-IR spectra.

**Figure 9.** Mechanical behaviors of electrodes and different binders, (a) Stress-strain measurement of the binder film on the slide glass, measuring the mechanical strength of PAA, PAA/Pullulan, PAA/Pullulan-CN, and PAA/CMC. (b) Adhesion characteristics of those binders in the electrode on the current collector, measured by peel test method. (c) The transference number of sodium ion ( $\text{Na}^+$ ) in each sodium symmetric cells containing 1.0 M  $\text{NaClO}_4$  with EC/PC (1:1 v/v) 10% FEC additive, Wittman<sup>tm</sup> glass fiber separators which are coated with different binders, reference(not coated, raw separator), PAA/pullulan-CN, PAA/pullulan, and PAA, respectively. (d) The Electrochemically active surface area (ECSA) and cyclic voltammograms of antimony electrodes were indicated The relationship between cathodic peak currents at **Figure 10a, b and c** ( $I_{pc}$ ) and the square root of the scan rate.

**Figure 10.** The cyclic voltammograms of antimony electrodes were indicated, with PAA, PAA/Pullulan and PAA/Pullulan-CN at the scan rate of (a) 0.2, (b) 0.6, and (c) 1.0  $\text{mV s}^{-1}$

**Figure 11.** Electrochemical performances of Sb electrodes with three different binders. (a) The first galvanostatic charge/discharge cycle of three electrodes with the condition of 0.05 C rate, potential range of 0.01 – 2.0 V (vs Na/Na<sup>+</sup>) showing with calculated initial coulombic efficiencies respectively. Cyclabilities of three electrodes which contain different binder each, by plotting cell discharge capacities versus cycle number during 200 cycles, at (b) 0.2 C/0.2 C charge/discharge or (c) 1 C/1 C.(d) Rate performances of three electrodes, plotting discharge capacities versus specific C rates, all C rate conditions were operated for same value of charge/discharge C rates during 5 cycles each, and after highest value of 20 C rate, return the C rate as 0.2 C. (1C = 660  $\text{mA g}^{-1}$ )

**Figure 12.** The comparison of rate performance which contains antimony electrodes were indicated, with different experimental method, mentioned in **Table 1**.

**Figure 13.** SEM images of Sb anode surfaces. The pristine SEM images of electrodes were captured after 12 hours in manufacturing. 1 C rate charge/discharge cycles containing different binders of (a) Poly-acrylic acid (PAA), (b) crosslinked PAA/Pullulan and (c) crosslinked PAA/Pullulan-CN at initial state, for Pristine, 1<sup>st</sup> sodiation, 1<sup>st</sup> desodiation, and 100<sup>th</sup> desodiation images. (1C = 660  $\text{mA g}^{-1}$ )

**Figure 14.** XPS analysis of three Sb electrodes vs Na metal, precycled for several numbers, measured by ESCALAB XPS. C 1s XPS spectra of Sb electrodes containing PAA, PAA/Pullulan, and PAA/CRS binder each, cycled after (a) 1cycles (b) 10 cycles for 0.05C/0.05C formation step then 1C/1C charge/discharge step ( $1C = 660 \text{ mA g}^{-1}$ ).

## List of Tables

**Table 1.** Comparing properties of Na(sodium) and Li(lithium) in secondary batteries

**Table 2.** The comparison with our works and other reported electrodes which containing antimony in the sodium ion battery anodes.

## List of Schemes

**Scheme 1.** Failure mechanisms of silicon anode electrode (a) material pulverization, (b) thick SEI growth by continuous SEI layer composition, and (c) morphology and volume change of the entire Si electrode.

**Scheme 2.** Four components of anode electrode; Brown plate = current collector, big gray sphere = active material, small black sphere = conductive additive, blue strand = binders.

**Scheme 3.** Intercalation comparison of Na<sup>+</sup> ion and Li<sup>+</sup> ion in the graphite.

**Scheme 4.** The nano-sized antimony particles were synthesized by chemical reduction reaction of SbCl<sub>3</sub>. 1.0 g of SbCl<sub>3</sub> is dissolved by 50 mL of ethanol, then mix it with 0.6 mg of NaBH<sub>4</sub> in ethanol solution at room temperature, at 150 rpm stirring. The reduction reaction lasts for 3 hours, then took vacuum filtration with D.I water and ethanol to harvest the resultant. After the filtration, dry antimony particles for 80 °C, vacuum condition, then insert the powder in the freeze dryer at -120 °C condition.

**Scheme 5.** schematic figure of binder-coated separator for measuring transference number.

**Scheme 6.** Graphical showing of the three binders and their cross-linking. (a) Chemical structures of three different polymer binder and their crosslinking dehydration reaction; Blue strands = Poly-acrylic acid (PAA); Red strands = Two kinds of polysaccharides, Pullulan or Pullulan-CN; White intersection = Crosslinked polymer binder network formed by dehydration reaction between Poly-acrylic acid and Pullulan or Pullulan-CN. (b) Increasing of sodium ion transfer around the electrode facilitated by pullulan-CN binder, comparing with PAA.

## Nomenclature

---

EVs	Electric vehicles
HEVs	Hybrid electric vehicles
PHEVs	Plugin hybrid electric vehicles
IoT	Internet of things
LIBs	Lithium ion batteries
Li	Lithium
Na	Sodium/Natrium
Si	Silicon
C	Carbon
Sb	Antimony
Sn	Tin
Ge	Germanium
SEI	Solid electrolyte interface
CMC	Carboxymethyl cellulose
Meldrum's acid	2,2-dimethyl-1,3-dioxane-4,6-dione
SIBs	Sodium ion batteries
PAA	Poly(acrylic acid)
Pullulan-CN	Cyanoethyl pullulan
PVA-CN	Cyanoethyl polyvinyl alcohol
ESS	Energy storage system
PVDF	Polyvinylidene fluoride
$\eta$	Coulombic efficiency
NaBH <sub>4</sub>	Sodium borohydride
SbCl <sub>3</sub>	Antimony trichloride
NMP	N-methyl-2-pyrrolidone
NaClO <sub>4</sub>	Sodium perchlorate
EC	Ethylene carbonate
PC	Propylene carbonate
FEC	Fluoroethylene carbonate
CVs	Cyclic voltammograms
$t_{\text{Na}^+}$	Sodium ion transference number
$\varepsilon$	Dielectric constant
ECSA	Electrochemical active surface area
FT-IR	Fourier-transform infrared spectroscopy

SEM	Scanning electron microscopy
XPS	X-ray photoelectron spectroscopy
C	C rate
Na <sub>2</sub> CO <sub>3</sub>	Sodium carbonate
PFM	Poly(9,9-dioctylfluorene-co-fluorenone-co-methylbenzoic ester)
I <sub>pc</sub>	Peak current
n	Number of transferred electron
C <sub>0</sub> <sup>*</sup>	Concentration of Na <sup>+</sup> ion
A	Electrode area
D	Diffusion coefficient of Na <sup>+</sup> ion
v	Scan rate
D.I water	Deionized water

---



## Chapter 1. Introduction

### 1.1 Importance of secondary batteries in the future

Development of the EVs (Electric vehicles), mobile IT device, IoT (internet of things) devices increased demand of secondary batteries. Moreover, due to the current environmental problems such as energy exhaust, global warming and air pollution, the demand for renewable energy to replace conventional fossil fuel systems has increased dramatically, and secondary batteries, the storage medium of renewable energy, were also of interest. Comparing with other rechargeable secondary batteries (Lead-acid, Nickel-Cadmium or Nickel-Metal-Hydroxide) LIBs (Li ion batteries) have higher energy density and lower weight. <sup>1</sup> (Figure 1) Furthermore, LIBs have low self-discharge, dispose easier comparing with lead acid and nickel-cadmium battery due to nontoxic atoms in LIBs. For these reasons, research interests and demands of LIBs will become increased in the future. (Figure 2). <sup>2, 8, 9</sup>

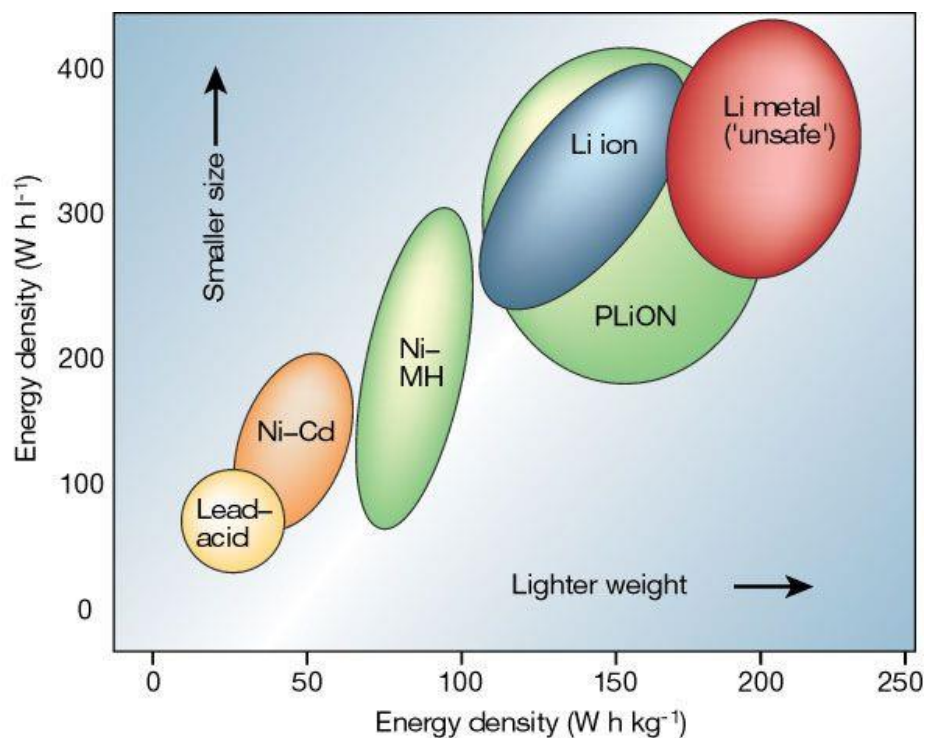
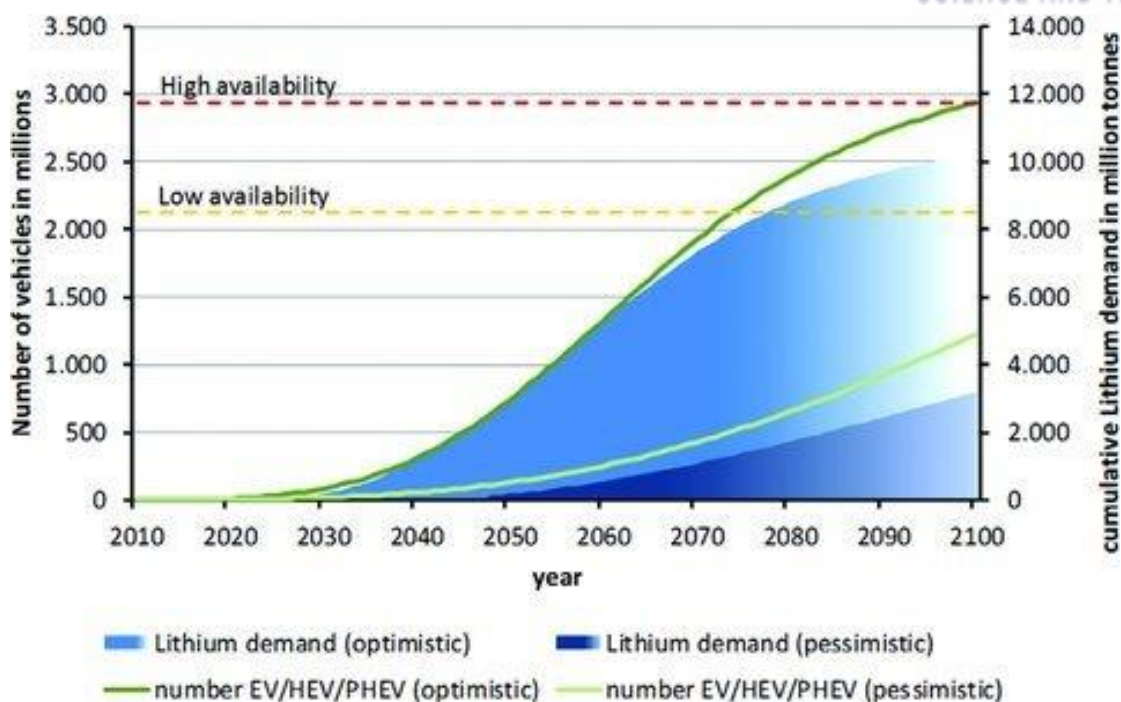


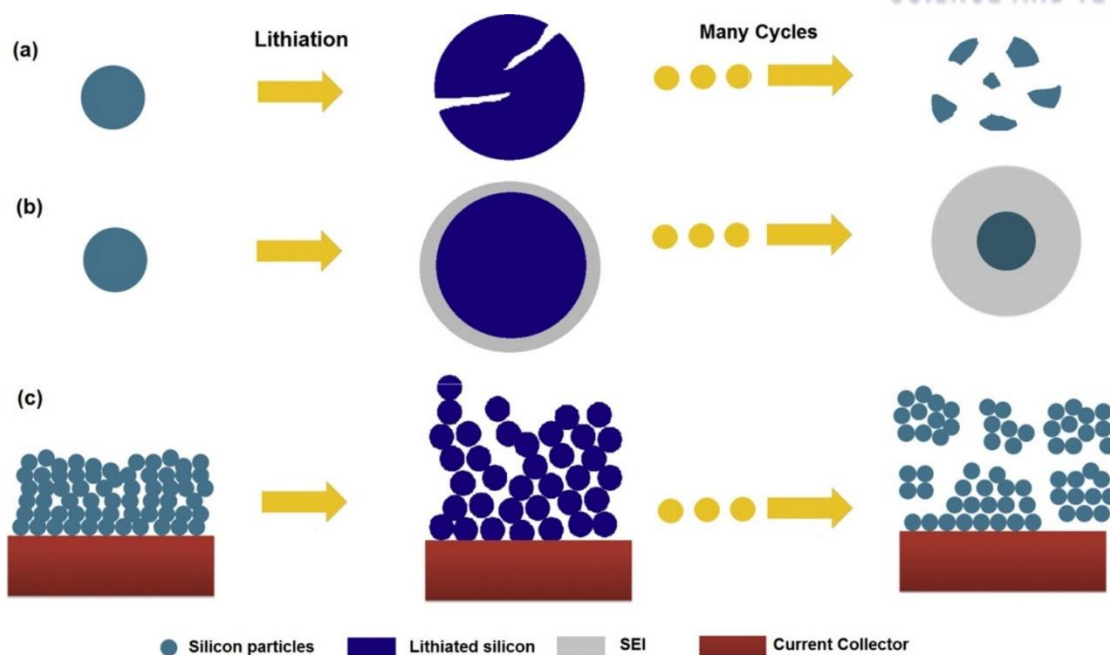
Figure 1. List of rechargeable batteries comparing with volumetric and gravimetric energy density. <sup>1</sup>



**Figure 2.** The number of Lithium demand, availability, electric vehicles (EVs), hybrid electric vehicles (HEVs) and plugin hybrid electric vehicles (PHEVs) over time. According to the availability of lithium and demand of EV/HEV/PHEV, run out of lithium the near future could be occurred. <sup>2</sup>

## 1.2 Introduction of alloy anode materials for lithium ion batteries (LIB)

The conventional anode material of LIBs is graphite, due to its reasonable cost, non-toxic property, abundance and proper theoretical capacity ( $372 \text{ mAh g}^{-1}$ ) by intercalation of Li ions during charge. <sup>8</sup> However, recent papers studied about the advanced anode materials to reach higher capacity comparing with graphite, such as Si (Silicon), Ge (Germanium), Sn (Tin), achieving high capacity by the alloying reactions: e.g,  $4200 \text{ mAh g}_{\text{Si}}^{-1}$  for  $\text{Li}_{4.4}\text{Si}$ ,  $1620 \text{ mAh g}_{\text{Si}}^{-1}$  for  $\text{Li}_{4.4}\text{Ge}$ ,  $994 \text{ mAh g}_{\text{Si}}^{-1}$  for  $\text{Li}_{4.4}\text{Sn}$ . However, these alloying materials showed huge volume expansion, (420% for  $\text{Li}_{4.4}\text{Si}$ , 400% for  $\text{Li}_{4.4}\text{Ge}$ , 360% for  $\text{Li}_{4.4}\text{Sn}$ ) and this volume expansion causes failure of electrode called pulverization. The pulverization of alloying materials causes three problems, (1) material pulverization (2) continuous SEI growth, (3) morphologic change of the entire Silicon electrode. **(Scheme 1)** <sup>10</sup> The repeated volume change along the lithiation/delithiation cycles encourages particle pulverization, isolating particles from electric pathways, breaking electrode integrity, exhausting electrolyte and triggering electrolyte decomposition on the fresh surface of pulverized anode materials.

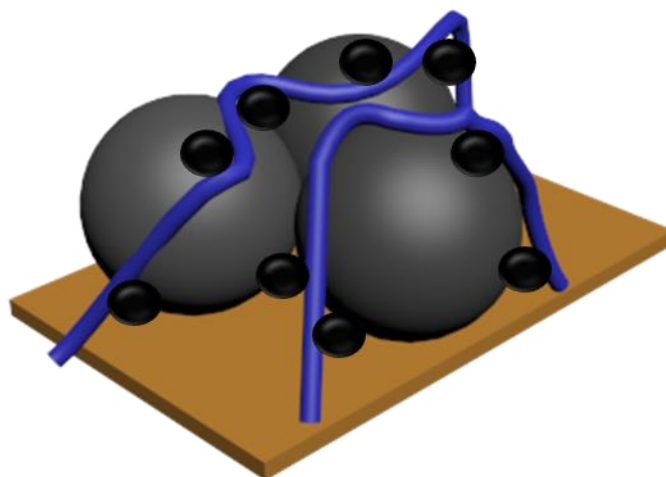


**Scheme 1.** Failure mechanisms of silicon anode electrode (a) material pulverization, (b) thick SEI growth by continuous SEI layer composition, and (c) morphology and volume change of the entire Si electrode.

Although this huge volume expansion of silicon in LIB anode system, but the merit of abundance, cheap cost and ten times higher theoretical capacity than graphite, pull the interest of researchers. This pulverization issue has been addressed by controlling the characteristic dimension of the anode materials (e.g., introducing porosity or adapting nanodimensional particles)<sup>11, 14-16</sup>, coating the active materials with conductive materials<sup>17-21</sup> and hybridizing the active materials with non-active materials.<sup>12, 22-24</sup>

### 1.2.1 Recent studies for binders to improve alloy anode materials in LIB system

The anode electrode consists of four representative components, current collector, active material, conductive additives and binders. Anode current collector assembles electrons at the outer conductor then supply electron to active materials, active materials make capacities by reacting with Li ions, conductive additives (such as carbon black) increase the conductivity of electrode. Adhesive and cohesive binders mainly used for binder, they connect current collector, active material and conductive agent then keep the integrity of electrode by adhesion (current collector - active material) and cohesion (active material – another active material or conducting agent).<sup>25</sup> (**Scheme 2**)



**Scheme 2.** Four components of anode electrode; Brown plate = current collector, big gray sphere = active material, small black sphere = conductive additive, blue strand = binders.

It has been reported that the volume change of the alloying-reaction-based anode materials and its following effects were suppressed by adopting binders having appropriate properties. Mechanically toughness polymeric binders such as alginate<sup>26</sup>, carboxymethyl cellulose (CMC)<sup>27</sup>, amylopectin<sup>28</sup> and pullulan<sup>4</sup>, are essential for keeping the electrode integrity and suppressing pulverization. Binders which form strong bonding with surface of active material such as poly(acrylic acid) (PAA)<sup>29</sup>, guar gum<sup>30</sup> and 5-methyl-5-(4-vinylbenzyl) Meldrum's acid<sup>31</sup> improved the reversibility of silicon due to the covalent bond or hydrogen bond between the binders and surface oxide of active material. Furthermore, the bi-polymer system of mechanically toughness polymer and strong bonding polymer, such as cross-linking of PAA with pectin<sup>3</sup>(**Figure 3**), CMC<sup>32</sup> or pullulan<sup>4</sup> (**Figure 4**) via condensation is essential to forming branched structure, reinforcing the mechanical strength and reversibility of the silicon. This branched architecture of bi-polymer binder systems provide more improved reversibility of lithiation/delithiation of silicon via interchain cohesion.<sup>33, 34</sup>



**Figure 3.** Polysaccharides polymeric binders characterized by glycosidic linkages between their monomeric units and functional moieties on side chains. (a) Molecular structures of polysaccharides: CMC, pectin. (b) Schematic figure of morphological changes of two polysaccharides binders and silicon particles along lithiation and delithiation: white strands = polymeric binders; red points = covalent bonds between hydroxyl and carboxylate moieties of binder; blue points = condensation reaction of between carboxylate of binders and hydroxyl moieties of silicon oxide films on the silicon particles.<sup>3</sup>

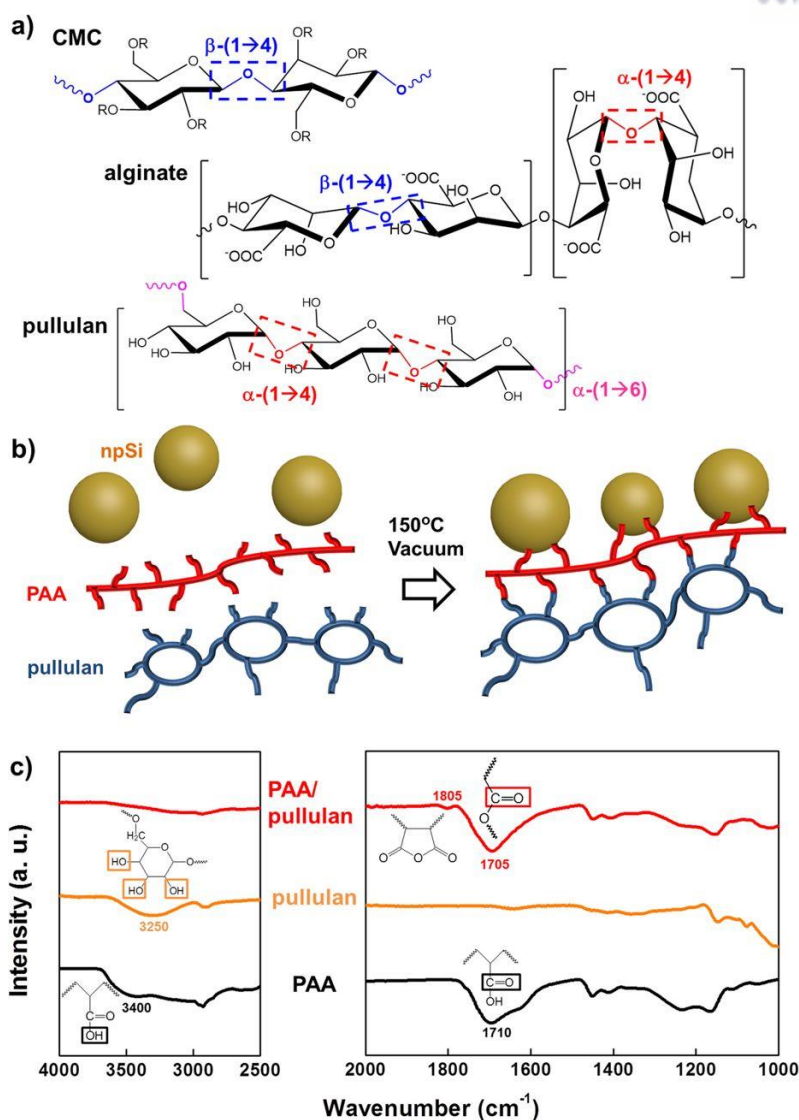


**Figure 4.** (a) Structure of alginate, CMC and pullulan. Glycosidic linkages ( $\alpha$ ,  $\beta$ ) of each polymeric binder were indicated. (b) Covalent condensation between surface oxide of Si and carboxylate of PAA as well as between pullulan and PAA after thermal heating at 150 °C. Dehydration reactions are induced at 150 °C between carboxylic moieties of PAA and hydroxyl moieties of pullulan and surface oxide of silicon. (c) FT-IR spectra of PAA, pullulan and PAA/pullulan, confirming the cross-linking of two binders by disappearance of hydroxyl moiety and appearance of ester moiety <sup>4</sup>

### 1.3 Comparison of LIB and sodium ion batteries (SIB)

The demands for LIBs were increased in past years, but the atomic ratio of Li in the crust of earth is not abundant. Moreover, the markets for large scale applications such as ESS (Energy storage system) were developed in present, but the expensive cost of LIBs are difficult to used for large-scale applications. Therefore, it is essential for developing alternative secondary batteries, which is free to abundance and cost problem, to replace the LIBs. Sodium is one of alkali metal, similar with Li, but it has low cost, infinite abundance in the earth. These characteristics of sodium triggers developing SIBs as an alternative to LIBs.<sup>2,35</sup> (Figure 5 and Table 1)

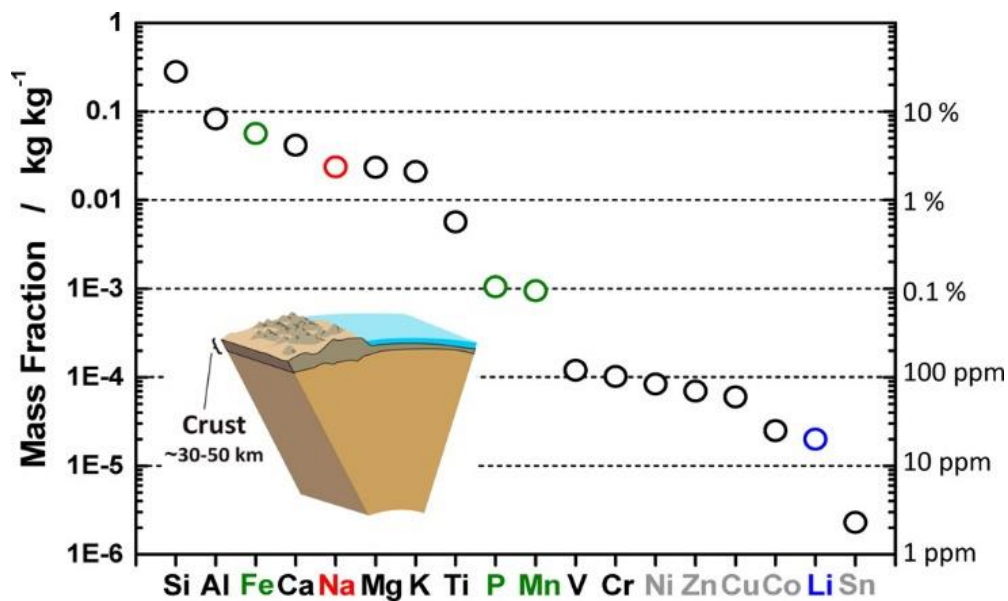


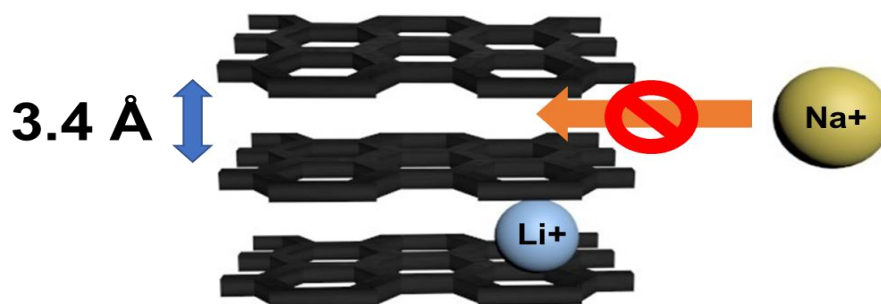
Figure 5. Natural abundance in the crust of earth. <sup>5</sup>

	Na	Li
Prices(for carbonates)	0.08 – 0.42 \$/kg	4.7 – 5.1 \$/kg
Voltage (vs SHE)	-2.71 V	-3.02 V
Capacity, metal	1165 mAh g <sup>-1</sup>	3829 mAh g <sup>-1</sup>
Cation radius	1.06 Å	0.76 Å

**Table 1.** Comparing properties of Na(sodium) and Li(lithium) in secondary batteries

## 1.4 Introduction of anode materials for SIB

However, because of the larger ionic radius of sodium, (1.03 Å versus 0.73 Å for Li<sup>+</sup>) sodium ions can't intercalate into the basal plane of graphite. <sup>36</sup> (**Scheme 3**) Therefore, SIB cannot use graphite as anode, require other anode materials.



**Scheme 3.** Intercalation comparison of Na<sup>+</sup> ion and Li<sup>+</sup> ion in the graphite.



Recent papers studied about the replacement of graphite, such as hard carbon, silicon, tin and antimony. However, there have been some problems reported for each of these alternative anode materials. The hard carbon can absorb sodium ion in its nanopores, but it was suffer with low volumetric capacity ( $450 \text{ mAh cm}^{-3}$ ) due to its low density. ( $1.5 \text{ g cm}^{-3}$ ). The tin forms binary alloy with sodium ion to  $\text{Na}_{15}\text{Sn}_4$ , showing very high gravimetric capacity. ( $847 \text{ mAh g}^{-1}$ ) However, tin suffers from pulverization during sodium alloying.<sup>37</sup> The Antimony (Sb) is promising alloying material for SIB anode, showing high gravimetric capacity through alloy reaction ( $660 \text{ mAh g}^{-1}$ ) and volumetric capacity ( $1120 \text{ mAh cm}^{-3}$ ) by forming  $\text{Na}_3\text{Sb}$ . However, like silicon and tin, too large amount of alkali metal is incorporated into the metals and metalloids so that severe volume expansion is inevitable: e.g., 393 % volume expansion from Sb to  $\text{Na}_3\text{Sb}$ .<sup>38,39</sup>

#### 1.4.1 Recent studies for binders to improve alloy anode materials in SIB system

Like the binder works for LIBs silicon anode mentioned at the previous page,<sup>3, 4, 26, 28, 29, 31, 32, 40</sup> binder works for sodiation alloy materials are in interest. Komaba et al.<sup>6</sup> introduced about the polyacrylate binder for Tin anode electrode, and Gao et al.<sup>41</sup> introduced about the cross-linked chitosan and glutaraldehyde for antimony. This binder works suppress the volume expansion of alloy materials, showing better cyclabilities comparing with conventional binders such as PVDF (Polyvinylidene fluoride) or non-crosslinked chitosan. **(Figure 6)**

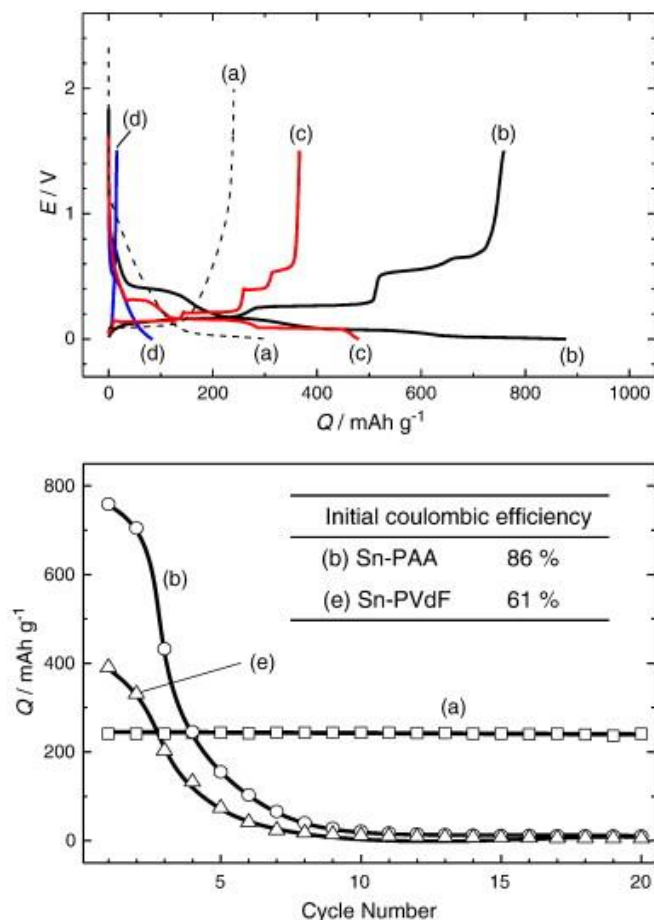


**Figure 6.** (upper) Initial charge and discharge profiles and (bottom) cyclability of (a) hard-carbon with PVdF binder, (b) Sn-PAA, (c) Pb-PAA, (d) Si-PAA, and (e) Sn-PVdF. The hard-carbon electrodes were characterized in beaker-type Na cells at  $25 \text{ mA g}^{-1}$ , and Sn, Pb, Si and Sn based electrodes were tested in coin-type cells at  $50 \text{ mA g}^{-1}$  in  $1.0 \text{ M NaClO}_4 \text{ PC}$ .<sup>6</sup>

#### 1.4.2 Other problems of SIBs anode and strategies to solve this problem

The size of sodium ion bigger than that of lithium ion ( $1.03 \text{ \AA}$  for  $\text{Na}^+$  versus  $0.73 \text{ \AA}$  for  $\text{Li}^+$ ) limits its mass transfer and charge transfer kinetics.<sup>36, 42, 43</sup> In addition to suppressing pulverization, therefore, it is useful to install an active transport mechanism of sodium ion into active materials. Dai et al.<sup>44</sup> introduced electroactive binder, PFM (Poly(9,9-dioctylfluorene-co-fluorenone-co-methylbenzoic ester)), to enhance the kinetics of tin nanoparticles in SIBs anode. For LIBs system, Hwang. et al.<sup>7</sup> demonstrated that cyanoethyl polyvinyl alcohol (PVA-CN) crosslinked with PAA played a role of increasing lithium ion transport number ( $t_{\text{Li}^+}$ ) to get better transfer kinetics comparing with PAA/CMC binder (good adhesion strength but no transfer kinetic enhancement).<sup>45</sup> **(Figure 7)** If

these approaches are applied at SIBs system, limited mass transfer and charge transfer kinetics will be solved.

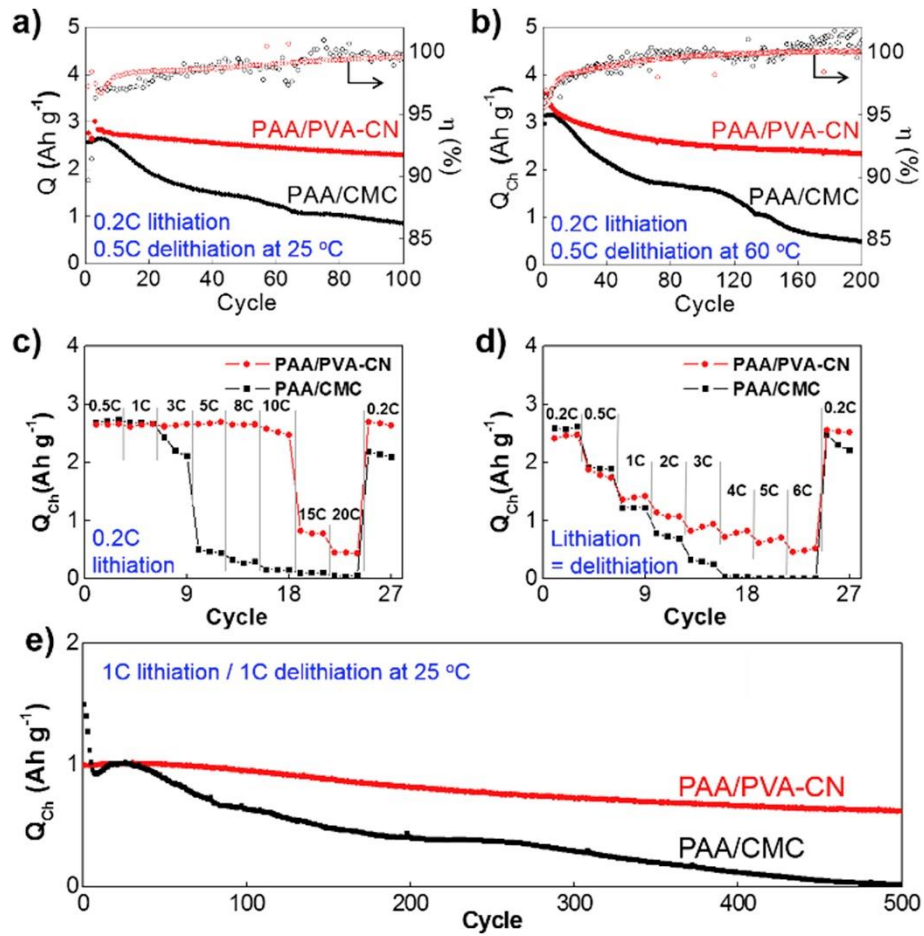


**Figure 7.** Electrochemical performance of PAA/PVA-CN or PAA/CMC binder-based silicon anodes. Cyclability and coulombic efficiency along continuous cycles of lithiation and delithiation at 25 °C (a) and 60 °C. (b) Rate performance of silicon anodes. Controlling delithiation of silicon anodes with lithiation fixed at 0.2 C (c) Same lithiation/delithiation C-rate were used for (d). Cyclability at 1 C/1 C cycles. (e) <sup>7</sup>

## Chapter 2. A crosslinked binder to enhance the performance of antimony anode for sodium-ion batteries

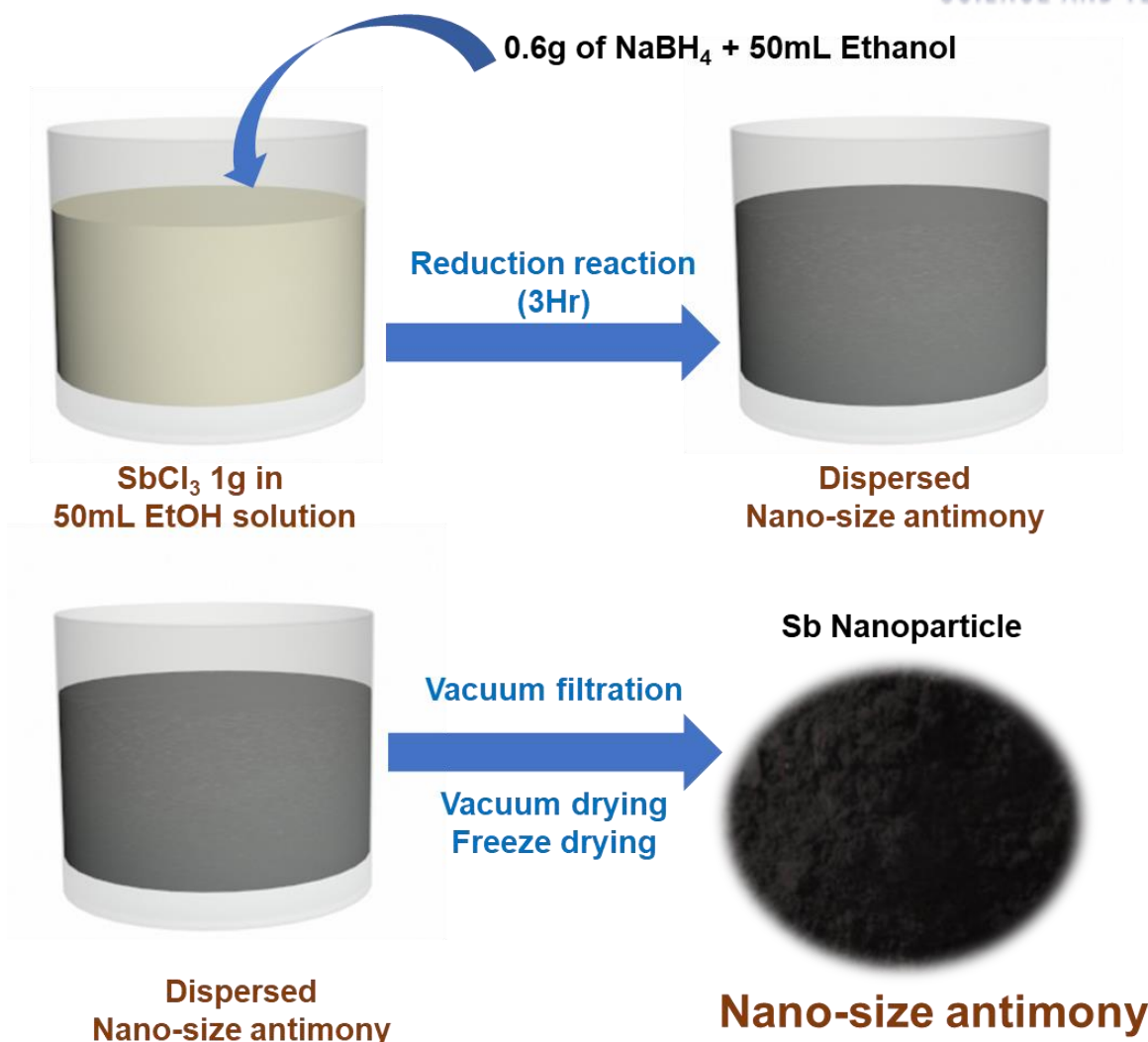
### 2.1. Introduction

In this work, we present a novel binder system composing of cyanoethyl pullulan (pullulan-CN) crosslinked with PAA for antimony-based SIBs. The polysaccharide backbone of pullulan-CN provides mechanical toughness to suppress the volume expansion of antimony during sodiation while the cyanoethyl groups of pullulan-CN facilitate sodium ion transport (high sodium ion transport number  $t_{\text{Na}^+}$ ). The dissolution of pullulan-CN in electrolyte was prevented by crosslinking pullulan-CN with PAA. The bi-polymer composite binder system (PAA/pullulan-CN) was compared with PAA and PAA/pullulan to decouple the effects of the mechanical toughness factor and transference number factor on cell performances. Resultantly, PAA/pullulan-CN drove antimony-based SIBs to work most reversibly along sodiation/desodiation cycles.

### 2.2 Experimental method and materials

#### 2.2.1 Binder & Antimony preparation.

Nano-size antimony (~200 nm) was prepared by reducing  $\text{Sb}^{3+}$  (**Scheme 4**). 0.6 g  $\text{NaBH}_4$  was introduced into 1 g  $\text{SbCl}_3$  in 50 ml ethanol for reduction reaction. The solution was stirred at 150 rpm for 3 h at room temperature. Sb particles were recovered and washed through vacuum filtration with excess ethanol and deionized water. The Sb particles were dried under vacuum at 120 °C and then freeze-dried at -120 °C (Operon FDCF-12012). Two different polymeric binder solutions were prepared. Pullulan (MW = 200,000; Sigma-Aldrich) or pullulan-CN (MW = 316,000; Shin-Etsu Chemical) was mixed with PAA (MW = 250,000; Sigma-Aldrich) at 8:2 wt. ratio in N-methyl-2-pyrrolidone (NMP) solvent at 80 °C.



**Scheme 4.** The nano-sized antimony particles were synthesized by chemical reduction reaction of SbCl<sub>3</sub>.<sup>41</sup> 1.0 g of SbCl<sub>3</sub> is dissolved by 50 mL of ethanol, then mix it with 0.6 mg of NaBH<sub>4</sub> in ethanol solution at room temperature, at 150 rpm stirring. The reduction reaction lasts for 3 hours, then took vacuum filtration with D.I water and ethanol to harvest the resultant. After the filtration, dry antimony particles for 80 °C, vacuum condition, then insert the powder in the freeze dryer at -120 °C condition.

### 2.2.2 Cell preparation

The 2032-coin-type configuration was used for the antimony-based SIB half cells, having sodium metal for counter electrode with the glass fiber membrane (Wattman) as the separator. The slurry of antimony particles, binder polymer and carbon black at 7 : 1.5 : 1.5 wt. ratio in NMP was loaded on copper foil at 1.0 mg cm<sup>-2</sup>. Then, the antimony electrodes were dried at 150 °C for 3 h in vacuum.

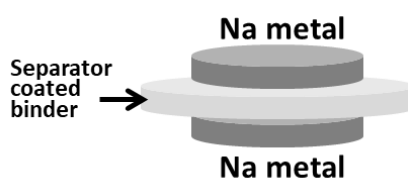
Thin sodium foil was used for counterpart of the antimony anode, by cutting and rolling sodium metal chunk (Sigma-Aldrich) about 10  $\mu\text{m}$  thickness. Glass-fiber separator (Wattman) was used for effective ion transport and prevent short circuit of cell. 1.0 M  $\text{NaClO}_4$  in EC/PC (1:1 v/v) with 10 wt. % FEC additive was used as electrolyte (EC = ethylene carbonate; PC = propylene carbonate; FEC = fluoroethylene carbonate). The assembled cells were located at 45 °C for 3 h before electrochemical characterization. Assembling coin type cells were assembled in Ar-filled glove box (MOTEK).

### 2.2.3 Mechanical characterization

Adhesion strength of 10  $\mu\text{m}$ -thick antimony composite electrodes was measured by 180° adhesive peel strength test described in ASTM D1876. Tensile strength of 50  $\mu\text{m}$ -thick binder films was measured by stretching the films by the tensile strength machine (Petrol LAB DA-01).

### 2.2.4 Electrochemical characterization.

The antimony-based SIB cells were charged/discharged between 0.01 and 2.0 V (WonATech WBCS3000). The first cycle was operated at 0.05C (33  $\text{mA g}^{-1}$ ) to form the stable SEI layer. Cyclic voltammograms (CVs) and Electrochemically active surface area (ECSA) were obtained by scanning potential at various scan rates (Biologic VMP). The transference number of sodium ion ( $t_{\text{Na}^+}$ ) were measured by the potentiostatic polarization method (VSP-300, BioLogic). Sodium metal symmetric cells were constructed with the glass fiber separator (Wattman) used in the SIB cells between the metals. The separator was coated with one of the tested binders (PAA, PAA/pullulan or PAA/pullulan-CN) by soaking the separator in the corresponding 10 wt. % binder solution and then drying at 150 °C for 3 h. (**Scheme 5**) The electrolyte used in SIB cells was injected to the sodium symmetric cells.



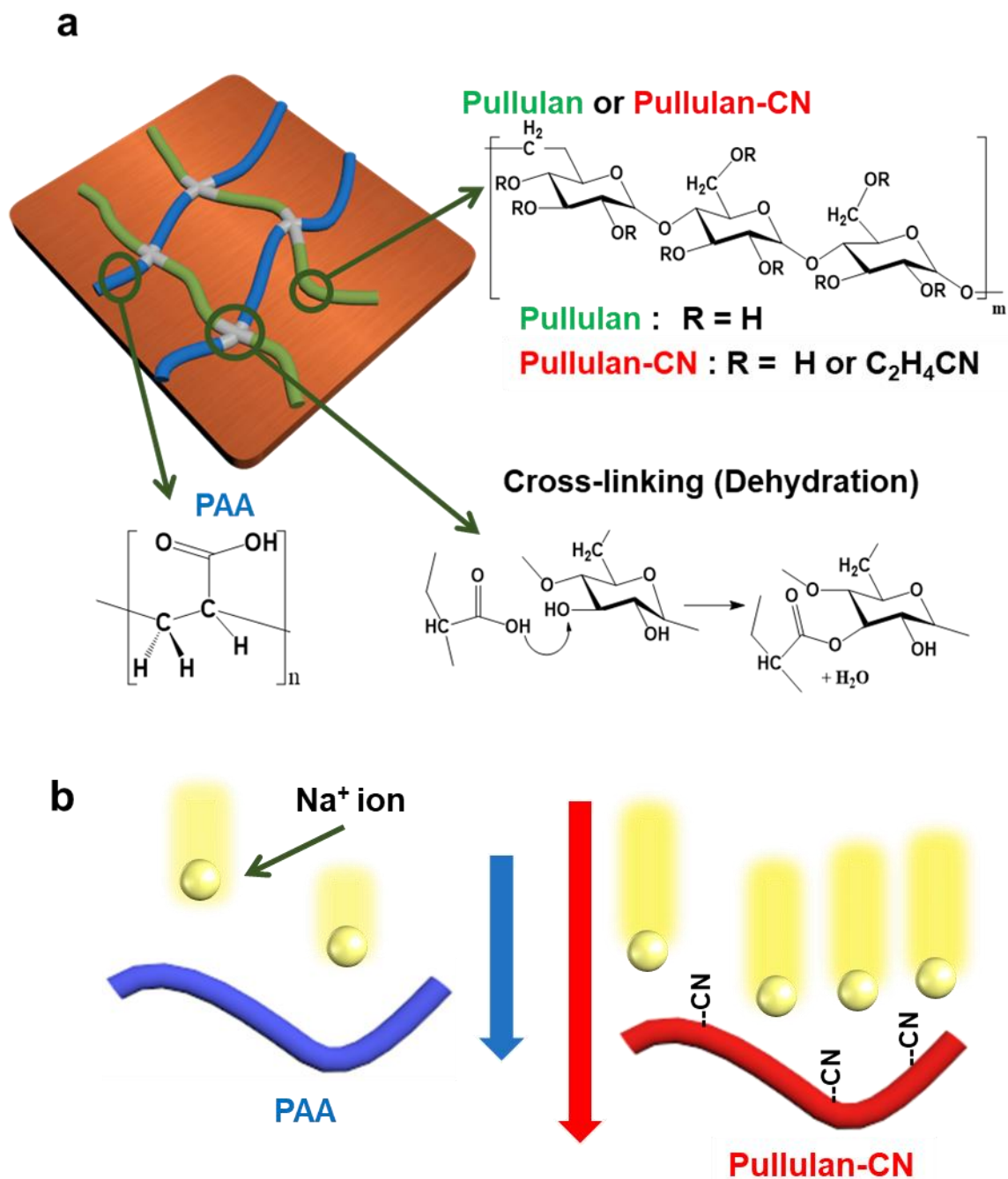
**Scheme 5.** schematic figure of binder-coated separator for measuring transference number.

### 2.2.5 Material characterization.

Functional groups of the binders were spectroscopically characterized by infrared (Bruker ALPHA). The microstructural morphology of antimony electrodes was investigated by the scanning electron microscopy (SEM; S-4800 Cold FE-SEM). The SEI layer of electrodes was characterized by the X-ray photoelectron spectroscope (XPS; ESCALAB 250XI) with C1s peak focusing.

## 2.3. Results and Discussion

The PAA/pullulan-CN-based antimony anodes were prepared to have the cross-linkage between PAA and pullulan-CN and strong bonds between PAA and antimony. The anode slurry containing antimony particles with PAA/pullulan-CN was coated on copper current collectors. Then, the anode was aged at 150 °C for 3 h. PAA was strongly bound to antimony surface as the condensation reaction of the carboxyl side chain of PAA and the hydroxyl moieties of the surface oxide of antimony<sup>16, 46</sup> proceeded at the aging temperature.<sup>29, 32, 47</sup> At the same time, PAA and pullulan-CN were crosslinked via the condensation reaction between the carboxyl moieties of PAA and the hydroxyl moieties of pullulan-CN (**Scheme 6a**).<sup>4</sup> Furthermore, the sodium ion (yellow balls at **Scheme 6b**) is strongly bound by the cyanoethyl moieties around the glucopyranosides. As a result, the ion transport around the electrode was improved.



**Scheme 6.** Graphical showing of the three binders and their cross-linking. (a) Chemical structures of three different polymer binder and their crosslinking dehydration reaction; Blue strands = Poly-acrylic acid (PAA); Red strands = Two kinds of polysaccharides, Pullulan or Pullulan-CN; White intersection = Crosslinked polymer binder network formed by dehydration reaction between Poly-acrylic acid and Pullulan or Pullulan-CN. (b) Increasing of sodium ion transfer around the electrode facilitated by pullulan-CN binder, comparing with PAA.



The chemical structure of binders and bipolymer condensation reaction were confirmed by IR spectra. Hydroxyl peak of the pullulan was observed, (dispersed around wavelength  $3304\text{ cm}^{-1}$ ) and smaller hydroxyl group peak of pullulan-CN was observed, (dispersed around wavelength  $3460\text{ cm}^{-1}$ ) because of replacing hydroxyl group to cyanoethyl groups. Nitrile functional groups of pullulan-CN and PAA/pullulan-CN were observed at the wavelength  $2250\text{ cm}^{-1}$ . The carboxylate peak of non-crosslinked PAA at  $1695\text{ cm}^{-1}$  is observed. When the bipolymer mixture of PAA and pullulan or pullulan-CN had gotten  $150\text{ }^{\circ}\text{C}$  under vacuum, carboxylate peak of PAA converted to ester group peak with the hydroxyl groups of pullulan or pullulan-CN. Thus, shifted ester group peak of PAA/pullulan or PAA/pullulan-CN was observed at  $1703\text{ cm}^{-1}$ , and hydroxyl group peak of pullulan or pullulan-CN was disappeared during the condensation reaction. <sup>4</sup> Moreover, two carboxylate moieties in the PAA react each other, making anhydride peak at  $1801\text{ cm}^{-1}$  (**Figure 8**). <sup>32</sup>

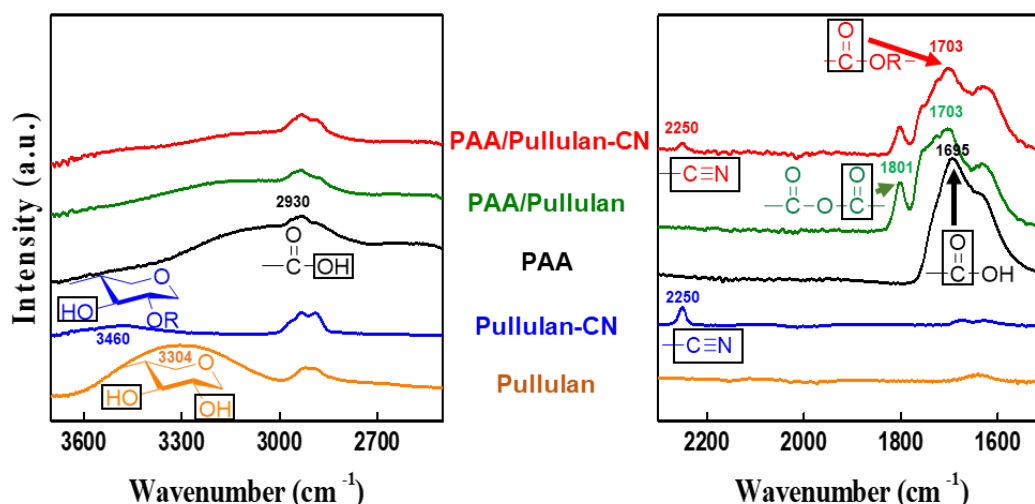


**Figure 8.** Structural informations about three polymers and their cross-linked bipolymers. The disappearance of hydroxyl and carboxylate moieties in the crosslinked polymers, appearance of ester moieties of cross-linked bi-polymer binders and remained nitrile groups measured by FT-IR spectra.

Mechanical properties of binders, such as stiffness and elasticity, were investigated since they affect the events of volume expansion and pulverization significantly (**Figure 9a**). The PAA film was easily elongated even by a small stress. The elastic modulus of PAA (1.03 MPa) was too small to resist against the volume expansion of antimony during sodiation. The PAA became mechanically stiffer after being cross-linked with polysaccharide: elastic modulus = 1.75 MPa for PAA/pullulan and 4.68 MPa for PAA/pullulan-CN. Both cross-linkage and higher elastic moduli of pullulan and pullulan-CN are responsible for the increase in mechanical stiffness. Dipole-dipole interaction of

nitrile groups encouraged PAA/pullulan-CN to be stiffer than PAA/pullulan.<sup>48</sup> However, both of the pullulan-based composite binders were less stiff than PAA/CMC (6.75 MPa) that is the binder popularly used for silicon anodes. The elasticity of pullulan backbone of pullulan-CN originates from the reversible chair-to-boat transition of pyranose unit of the polysaccharide on elongation.<sup>3,49</sup> The  $\alpha$ -glycosidic linkages of pullulan allows the molecular-level conformational change while the conformation of polysaccharide based on  $\beta$ -glycosidic linkages such as CMC is fixed at chair even after elongation. In our previous work, a more durable operation of silicon LIB was demonstrated by using pullulan crosslinked with PAA (PAA/pullulan) instead of the popularly used PAA/CMC. The PAA/pullulan let antimony anodes breathe in and out lithium ions with volume change rather than by fixing their dimensions.

Adhesion and cohesion of PAA/pullulan-CN were investigated by peeling off the Sb-containing active layers loaded on copper foil from the foil by using the 3M Magic tape (**Figure 9b**). The active layer containing PAA/pullulan-CN was most hardly detached, indicating the strongest adhesion. The minimum strength after the peel-off point was: 0.65 N/mm for PAA/pullulan-CN; 0.41 N/mm for PAA/pullulan; 0.18 N/mm for PAA. All the mass of active layer based on PAA/pullulan-CN was detached from the foil and found on the 3M Magic tape after the peel-off. It confirmed that the PAA/pullulan-CN guaranteed the strong cohesion between electrode components (antimony and carbon black) and therefore the electrode integrity. However, the pullulan-absent and cyanoethyl-absent binders (PAA and PAA/pullulan, respectively) showed lower and uneven peel strength. Only a portion of the mass of the active layer left on the 3M Magic tape confirmed their poor cohesion strength. It was reported that the nitrile pendants of polyarylene ether nitrile played a role of enhancing its adhesion ability due to their polar interaction.<sup>48,50,51</sup>

From the viewpoint of ionics, the PAA/pullulan-CN showed the highest transference number of sodium ion ( $t_{\text{Na}^+}$ ; **Figure 9c**): 0.68 for PAA/pullulan-CN versus 0.49 for its cyanoethyl-absent counterpart (PAA/pullulan) and 0.38 for its pullulan-absent counterpart (PAA). The cyanoethyl groups would be partly responsible for the high  $t_{\text{Na}^+}$  value. It was reported that the solvated sodium ion is more loosely bound to the cyanoethyl groups than its counter-anion, perchlorate.<sup>45,52-57</sup> The high  $t_{\text{Na}^+}$  supports high concentration of sodium ions nearby antimony particles during sodiation. The concentration polarization observed especially at the end of fast charging is possibly relieved because the lack of charge carriers nearby electrodes is solved in such a high  $t_{\text{Na}^+}$  environment. Also, high dielectric constant of pullulan-CN ( $\epsilon = 19$  for pullulan-CN<sup>58,59</sup> versus about 9.4 for pullulan<sup>60</sup> at 20 °C) possibly encourage the desolvation of sodium ions. The cyanoethyl side chains of the pullulan-CN binder plays an important role to increase the dielectric constant. This mechanism to reduce the

desolvation activation energy possibly improves the charge transfer kinetics of sodiation, guaranteeing good rate performances.

The superiority of transference number and desolvation capability of PAA/pullulan-CN supported full utilization of active mass of antimony in composite electrodes. Cyclic voltammograms of antimony anodes in half cells were compared between binders (**Figure 10**). Two cathodic processes of sodiation of antimony were identified at 0.39 V and 0.65 V.<sup>61, 62</sup> Higher currents were obtained from the PAA/pullulan-CN-based antimony anode than its controls. Electrochemical active surface area (ECSA) was calculated by Randles-Sevcik equation,

$$I_{pc} = (2.69 \times 10^5) n^{2/3} C_0^* A D^{1/2} \nu^{1/2}$$

where  $I_{pc}$  = peak current at a given potential,  $n^{2/3}$  = number of transferred electron (1 for  $\text{Na}^+$ ),  $D$  is diffusion coefficient of  $\text{Na}^+$  ion,  $C_0^*$  = concentration of the  $\text{Na}^+$  ion. estimated from the slope of Randles-Sevcik plots (peak current at 0.39 V versus the root square of scan rate).

The ECSA of PAA/pullulan-CN-based electrode is about 1.5 times larger than that of PAA/pullulan or PAA-based electrode. The control binders showed the similar value of ECSA. (**Figure 9d**)

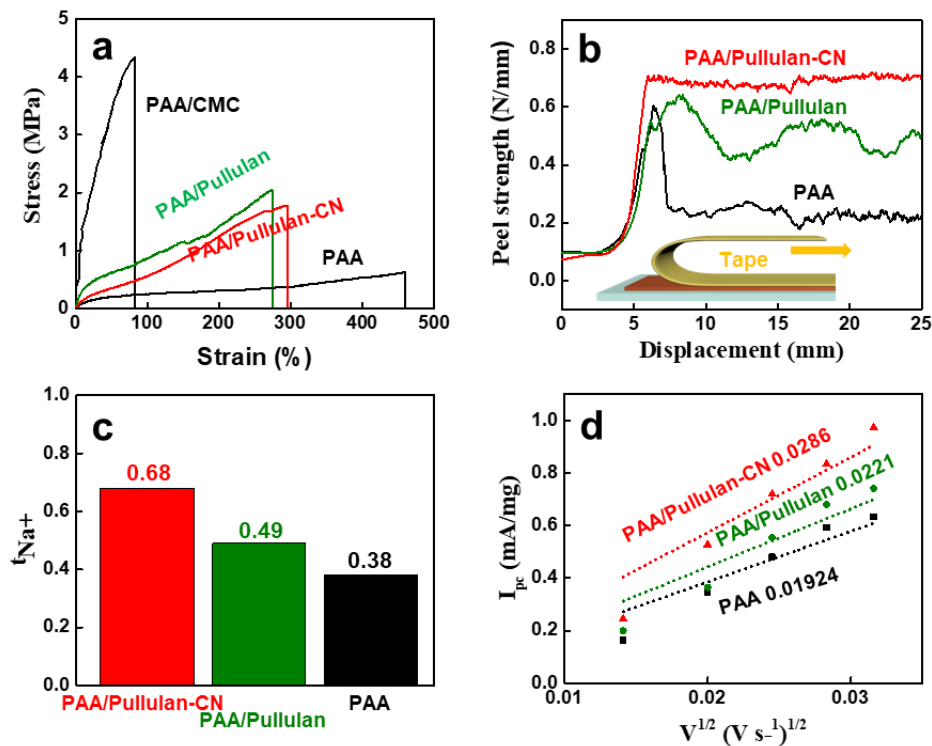


**Figure 9.** Mechanical behaviors of electrodes and different binders, (a) Stress-strain measurement of the binder film on the slide glass, measuring the mechanical strength of PAA, PAA/Pullulan, PAA/Pullulan-CN, and PAA/CMC. (b) Adhesion characteristics of those binders in the electrode on the current collector, measured by peel test method. (c) The transference number of sodium ion ( $\text{Na}^+$ ) in each sodium symmetric cells containing 1.0 M  $\text{NaClO}_4$  with EC/PC (1:1 v/v) 10% FEC additive , Wittman<sup>tm</sup> glass fiber separators which are coated with different binders, reference(not coated, raw separator) , PAA/pullulan-CN , PAA/pullulan, and PAA, respectively. (d) The Electrochemically active surface area (ECSA) and cyclic voltammograms of antimony electrodes were indicated the relationship between cathodic peak currents at **Figure 10a, b and c** ( $I_{pc}$ ) and the square root of the scan rate.

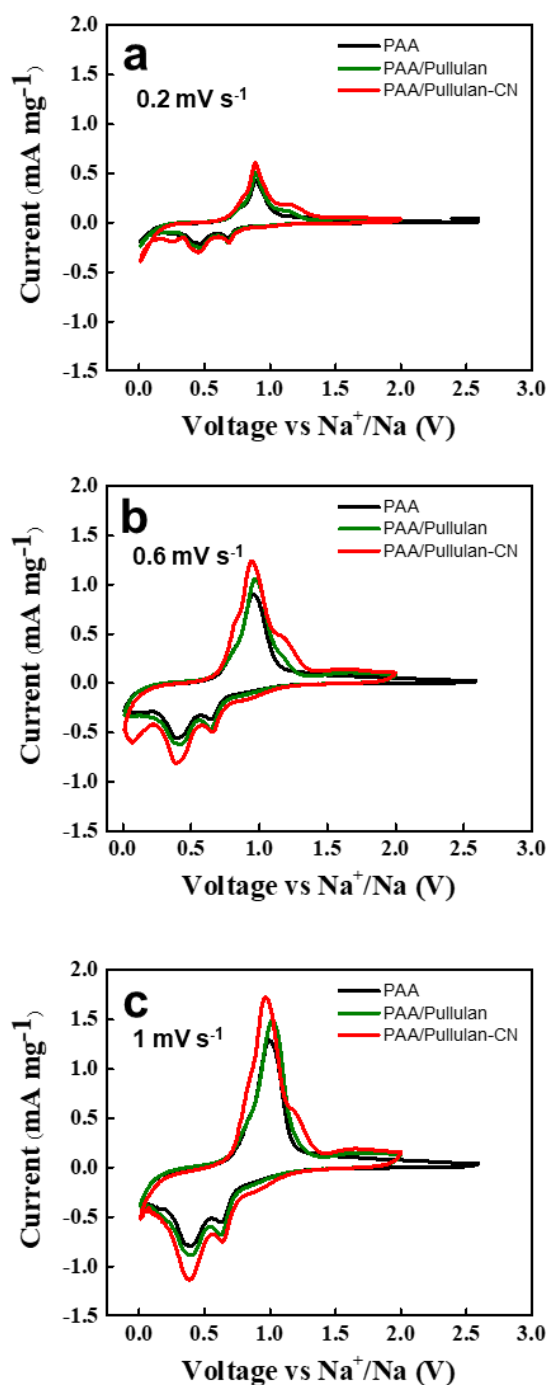


**Figure 10.** The cyclic voltammograms of antimony electrodes were indicated, with PAA, PAA/Pullulan and PAA/Pullulan-CN at the scan rate of (a) 0.2, (b) 0.6, and (c) 1.0 mV s<sup>-1</sup>

Considering its balanced mechanical properties between stiffness and elasticity, strong adhesion/cohesion, high transference number and high dielectric constant, we tested SIB half cells

galvanostatically by using the PAA/pullulan-CN binder. The sodiation and desodiation plateaus were found at 0.6 V and 0.9 V in all cells independent of binders (**Figure 11a**). The highest initial coulombic efficiency was obtained from PAA/pullulan-CN when compared with the controls: 70% for PAA/pullulan-CN > 69% for PAA/pullulan > 63% for PAA. The PAA/pullulan-CN was also superior to its controls in terms of cyclability at both 0.2C and 1C (**Figure 11b and c**). The cells containing pullulan-CN showed good capacity retention at least up to the 200<sup>th</sup> cycle. However, the cells based on the other two binders did not work at the cycle. The effects of high transference number and high dielectric constant of the binder were clearly shown. The capacity difference between the pullulan-CN-present and absent binders became more emphasized as the current (C-rate) increased (**Figure 11d**). The capacity decay of the pullulan-CN-containing cells was not very serious along C rates: 55.9 % of the capacity at 0.2C was achieved at 20C. On the other hand, a meaningful capacity was not extracted at 20C from the control binder cells.

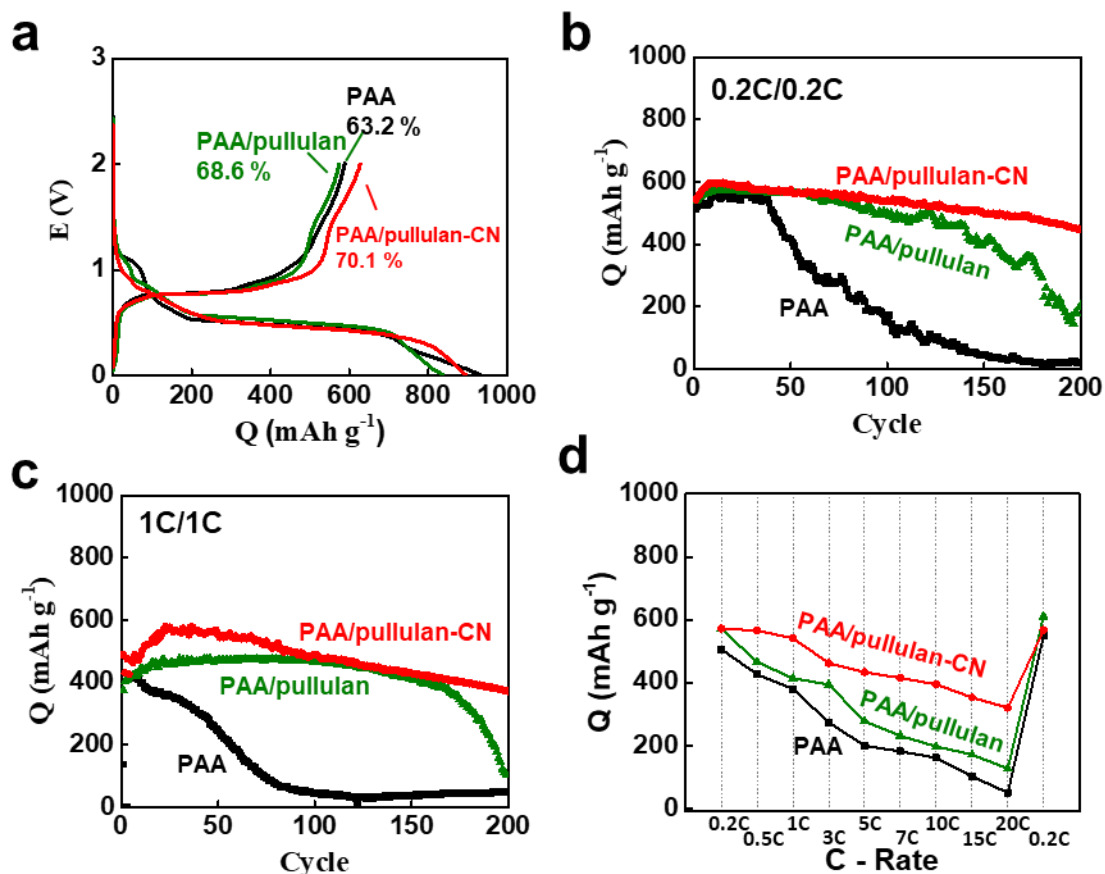


**Figure 11.** Electrochemical performances of Sb electrodes with three different binders. (a) The first galvanostatic charge/discharge cycle of three electrodes with the condition of 0.05 C rate, potential range of 0.01 – 2.0 V (vs Na/Na<sup>+</sup>) showing with calculated initial coulombic efficiencies respectively. Cyclabilities of three electrodes which contain different binder each, by plotting cell discharge

capacities versus cycle number during 200 cycles, at (b) 0.2 C/0.2 C charge/discharge or (c) 1 C/1 C. (d) Rate performances of three electrodes, plotting discharge capacities versus specific C rates, all C rate conditions were operated for same value of charge/discharge C rates during 5 cycles each, and after highest value of 20 C rate, return the C rate as 0.2 C. (1C = 660 mA g<sup>-1</sup>)

The rate capability obtained from the PAA/pullulan-CN cells is considered most excellent when compared with those of previously reported works (**Table 2 and Figure 12**).

Materials	Initial capacity (mAh g <sup>-1</sup> )	C rate	Capacity at Highest C rate (mAh g <sup>-1</sup> )	Capacity retention (%)
Sb electrode with PAA/Pullulan-CN binder (This work)	571.46	20	319.17	55.85 %
Sb@C coaxial nanotubes <sup>18</sup>	948	21.10	310	32.70 %
Sb nanorod array <sup>62</sup>	~950	21.05	557.7	58.71 %
Sb hollow nanosphere <sup>11</sup>	~628	2.42	315	50.16 %
Nanoporous antimony <sup>15</sup>	~610	5	420	68.85 %
Cypress leaf-like Sb porous hollow microsphere <sup>14</sup>	639	4.85	312.9	48.96 %
Bulk Sb <sup>63</sup>	~600	4	491	81.83 %
Sb/C fibers <sup>64</sup>	405	9.1	88	21.73 %
Nanocomposite Sb/C <sup>65</sup>	624	3.03	309	49.52 %

Sb-C nanofibers <sup>66</sup>	631	5	337	53.41 %
Rod-like Sb-C composite <sup>67</sup>	499.8	0.38	259.1	51.84 %
Antimony/graphitic carbon composite <sup>68</sup>	310	10	202	65.16 %
Spherical nano Sb@C composites <sup>69</sup>	420	15.15	146	34.76 %

**Table 2.** The comparison with our works and other reported electrodes which containing antimony in the sodium ion battery anodes.

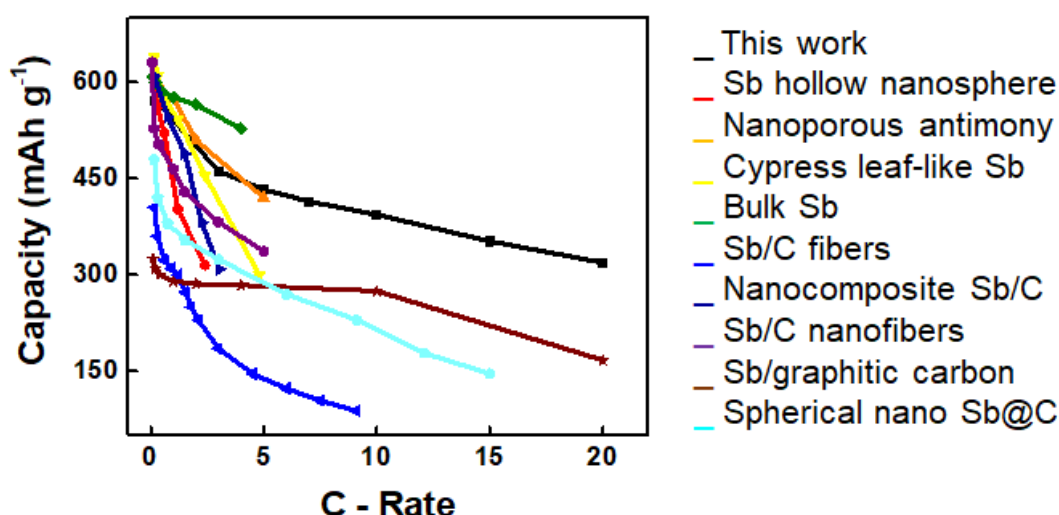


**Figure 12.** The comparison of rate performance which contains antimony electrodes were indicated, with different experimental method, mentioned in **Table 1**.

The morphological change of antimony electrodes was traced along sodiation and desodiation (**Figure 13**). In the presence of PAA as the binder for antimony electrode (**Figure 13a**), the 11.8  $\mu\text{m}$ -thick electrode was thickness-expanded more than 2 times after the first sodiation. The original thickness was not fully recovered after the following desodiation. The thickness expansion at 123% (14.5  $\mu\text{m}$ /11.8  $\mu\text{m}$ ) was not reversible. After 100 times repeated sodiation followed by desodiation, the thickness of PAA electrode reached 21  $\mu\text{m}$  with macroscopic cracks developed. As expected from its



low elastic modulus and weak cohesion capability, the PAA did not keep the electrode integrity and therefore showed poor electrochemical performances. On the other hand, the thickness expansion of the bi-polymer-crosslinked binders after the first sodiation was not as serious as that of the PAA electrode (**Figure 13b and c**). Their original thicknesses were almost or fully recovered (especially for PAA/pullulan-CN) after the following desodiation. The electrodes based on the pullulan-related binders (thinner than 14  $\mu\text{m}$ ) were much thinner than the PAA electrode (thicker than 20  $\mu\text{m}$ ) after the 100<sup>th</sup> sodiation/desodiation cycles.

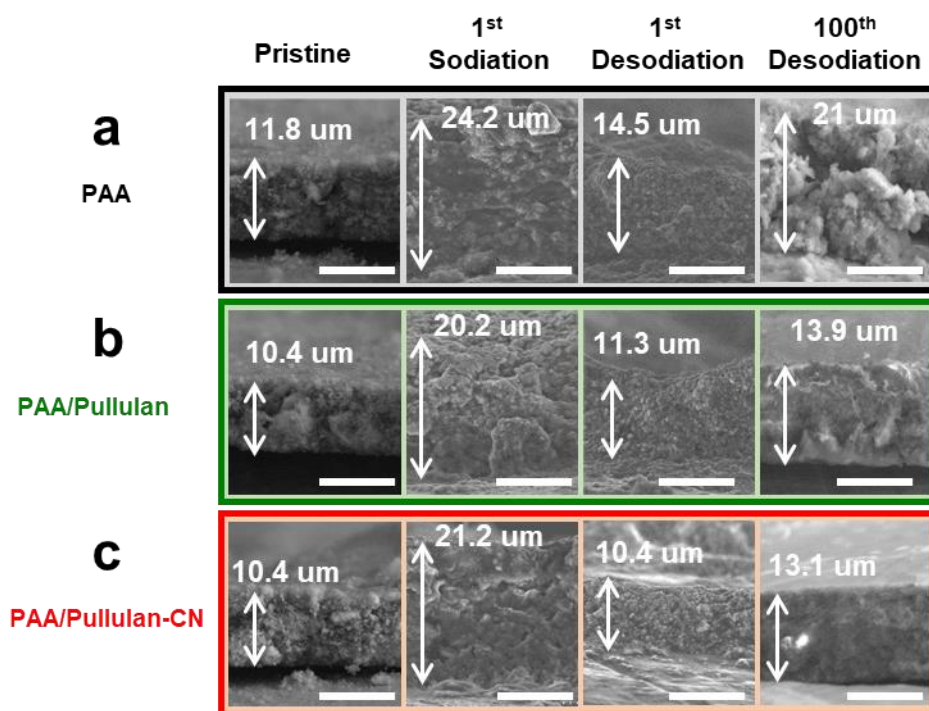


**Figure 13.** SEM images of Sb anode surfaces. The pristine SEM images of electrodes were captured after 12 hours in manufacturing. 1 C rate charge/discharge cycles containing different binders of (a) Poly-acrylic acid (PAA), (b) crosslinked PAA/Pullulan and (c) crosslinked PAA/Pullulan-CN at initial state, for Pristine, 1<sup>st</sup> sodiation, 1<sup>st</sup> desodiation, and 100<sup>th</sup> desodiation images. (1C = 660 mA g<sup>-1</sup>)

For better understanding on the excellent capacity retention even at fast charge and discharge performance, X-ray photoelectron spectroscopy (XPS) was performed to identify the components of the SEI layer at the electrode after the cycle used in each binder. The component of SEI layer was compared with after formation and 10 cycle. (**Figure 14a and b**) The surface of the electrodes featured five split peaks at C1s (the C-C single bond at 284.8 eV, the ether bond (-COC-) at 286.15 eV, the ester bond (-COOR-) at 288.4 eV, the carboxylate group (-COOH) peak at 289.5 eV and/or the Na<sub>2</sub>CO<sub>3</sub> peak at 290.3 eV.<sup>70-72</sup> The surface of PAA/Pullulan-CN based electrode featured less

carbonated contents in its SEI layer (288.4 and 290.3 eV), compare with PAA and PAA/Pullulan: % area of the carbonate peak = 14.30 % for PAA/pullulan-CN, 14.91 % for PAA/pullulan and 18.71 % for PAA after 10 cycle (**Figure 14**). The carbonate components were formed in SEI layer form EC molecules existing in electrolyte are reduced. The initial SEI layer was made of FEC (fluorinated EC), which was used as an SEI layer forming additive in this operation, so lower levels of carbonate are involved. Therefore, a relatively high carbonate content indicates decomposition of additional EC molecules. The new surface of antimony exposed to EC-based electrolytes developed with cracking during repetitive cycles accounts for the high carbonate content observed in PAA and PAA/Pullulan based electrodes. Basis of the results, the high  $t_{Na^+}$  help to guarantee health SEI layer, resulting in stable and fast electrochemical performance.<sup>71, 73, 74</sup>

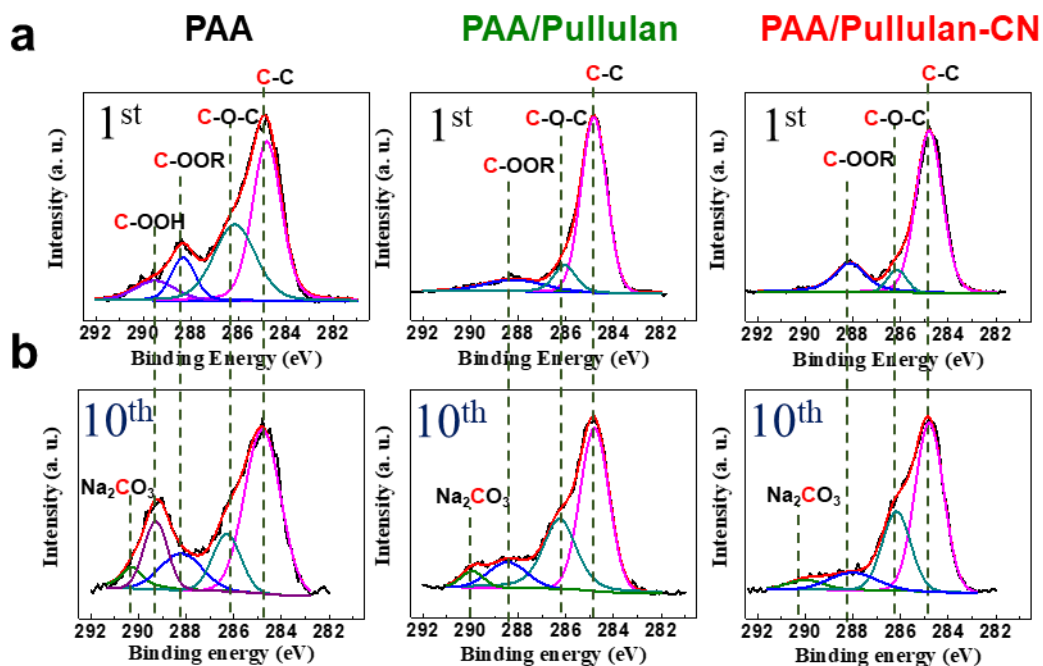


**Figure 14.** XPS analysis of three Sb electrodes vs Na metal, precycled for several numbers, measured by ESCALAB XPS. C 1s XPS spectra of Sb electrodes containing PAA, PAA/Pullulan, and PAA/CRS binder each, cycled after (a) 1cycles (b) 10 cycles for 0.05C/0.05C formation step then 1C/1C charge/discharge step (1C = 660 mA g<sup>-1</sup>).

## 2.4 Conclusion

In this work, we presented PAA/pullulan-CN as the effective binder for antimony anode of SIBs. Two characteristics (bond formation of PAA and ion transport, proper mechanical strength of pullulan-CN) of the bi-polymer-crosslinked binder system improved the reversibility and kinetics of sodiation/desodiation of antimony. Its balanced mechanical strength between stiffness and elasticity inhibited the volume expansion (thickness change <130% for PAA/pullulan-CN versus 180 % for PAA at the 100<sup>th</sup> cycle of 1C/1C) as well as pulverization, guaranteeing the capacity retention along cycles (*reversibility gain*: capacity at the 200<sup>th</sup> cycle of 1C/1C = 400 mAh g<sup>-1</sup> for PAA/pullulan-CN versus meaningless capacity for PAA). Also, its high sodium ion transference number ( $t_{\text{Na}^+} = 0.68$  for PAA/pullulan-CN versus 0.49 for PAA/pullulan) provided the sodium-ion-rich environments around antimony with lower desolvation activation required, supporting high rate performance (*kinetic gain*: capacity at 20C = 320 mAh g<sup>-1</sup> for PAA/pullulan-CN versus 122 mAh g<sup>-1</sup> for PAA/pullulan).

## 2.5 Reference

1. Tarascon, J.-M.; Armand, M., Issues and challenges facing rechargeable lithium batteries. In *Materials for Sustainable Energy: A Collection of Peer-Reviewed Research and Review Articles from Nature Publishing Group*, World Scientific: 2011; pp 171-179.
2. Slater, M. D.; Kim, D.; Lee, E.; Johnson, C. S., Sodium-Ion Batteries. *Advanced Functional Materials* **2013**, *23* (8), 947-958.
3. Yoon, D. E.; Hwang, C.; Kang, N. R.; Lee, U.; Ahn, D.; Kim, J. Y.; Song, H. K., Dependency of Electrochemical Performances of Silicon Lithium-Ion Batteries on Glycosidic Linkages of Polysaccharide Binders. *ACS Appl Mater Interfaces* **2016**, *8* (6), 4042-7.
4. Hwang, C.; Joo, S.; Kang, N. R.; Lee, U.; Kim, T. H.; Jeon, Y.; Kim, J.; Kim, Y. J.; Kim, J. Y.; Kwak, S. K.; Song, H. K., Breathing silicon anodes for durable high-power operations. *Sci Rep* **2015**, *5*, 14433.
5. Carmichael, R. S., *Practical Handbook of Physical Properties of Rocks and Minerals (1988)*. CRC press: 2017.
6. Komaba, S.; Matsuura, Y.; Ishikawa, T.; Yabuuchi, N.; Murata, W.; Kuze, S., Redox reaction of Sn-polyacrylate electrodes in aprotic Na cell. *Electrochemistry Communications* **2012**, *21*, 65-68.
7. Hwang, C.; Cho, Y.-G.; Kang, N.-R.; Ko, Y.; Lee, U.; Ahn, D.; Kim, J.-Y.; Kim, Y.-J.; Song, H.-K., Selectively accelerated lithium ion transport to silicon anodes via an organogel binder. *Journal of Power Sources* **2015**, *298*, 8-13.
8. Winter, M.; Besenhard, J. O.; Spahr, M. E.; Novak, P., Insertion electrode materials for rechargeable lithium batteries. *Advanced materials* **1998**, *10* (10), 725-763.
9. Armand, M.; Tarascon, J. M., Building better batteries. *Nature* **2008**, *451* (7179), 652-7.
10. Wu, H.; Cui, Y., Designing nanostructured Si anodes for high energy lithium ion batteries. *Nano Today* **2012**, *7* (5), 414-429.
11. Hou, H.; Jing, M.; Yang, Y.; Zhu, Y.; Fang, L.; Song, W.; Pan, C.; Yang, X.; Ji, X., Sodium/Lithium storage behavior of antimony hollow nanospheres for rechargeable batteries. *ACS Appl Mater Interfaces* **2014**, *6* (18), 16189-96.
12. Wang, N.; Bai, Z.; Qian, Y.; Yang, J., Double-Walled Sb@TiO<sub>2</sub>-x Nanotubes as a Superior High-Rate and Ultralong-Lifespan Anode Material for Na-Ion and Li-Ion Batteries. *Adv Mater* **2016**, *28* (21), 4126-33.
13. Zhou, X.; Dai, Z.; Bao, J.; Guo, Y.-G., Wet milled synthesis of an Sb/MWCNT nanocomposite for improved sodium storage. *Journal of Materials Chemistry A* **2013**, *1* (44).
14. Hou, H.; Jing, M.; Zhang, Y.; Chen, J.; Huang, Z.; Ji, X., Cypress leaf-like Sb as anode material for high-performance sodium-ion batteries. *Journal of Materials Chemistry A* **2015**, *3* (34), 17549-17552.
15. Liu, S.; Feng, J.; Bian, X.; Liu, J.; Xu, H., The morphology-controlled synthesis of a nanoporous-antimony anode for high-performance sodium-ion batteries. *Energy & Environmental Science* **2016**, *9* (4), 1229-1236.
16. Yang, Y.; Yang, X.; Zhang, Y.; Hou, H.; Jing, M.; Zhu, Y.; Fang, L.; Chen, Q.; Ji, X., Cathodically induced antimony for rechargeable Li-ion and Na-ion batteries: The influences of hexagonal and amorphous phase. *Journal of Power Sources* **2015**, *282*, 358-367.
17. Hu, L.; Zhu, X.; Du, Y.; Li, Y.; Zhou, X.; Bao, J., A Chemically Coupled

Antimony/Multilayer Graphene Hybrid as a High-Performance Anode for Sodium-Ion Batteries. *Chemistry of Materials* **2015**, *27* (23), 8138-8145.

18. Liu, Z.; Yu, X.-Y.; Lou, X. W.; Paik, U., Sb@C coaxial nanotubes as a superior long-life and high-rate anode for sodium ion batteries. *Energy & Environmental Science* **2016**, *9* (7), 2314-2318.

19. Qiu, S.; Wu, X.; Xiao, L.; Ai, X.; Yang, H.; Cao, Y., Antimony Nanocrystals Encapsulated in Carbon Microspheres Synthesized by a Facile Self-Catalyzing Solvothermal Method for High-Performance Sodium-Ion Battery Anodes. *ACS Appl Mater Interfaces* **2016**, *8* (2), 1337-43.

20. Wu, T.; Hou, H.; Zhang, C.; Ge, P.; Huang, Z.; Jing, M.; Qiu, X.; Ji, X., Antimony Anchored with Nitrogen-Doping Porous Carbon as a High-Performance Anode Material for Na-Ion Batteries. *ACS Appl Mater Interfaces* **2017**, *9* (31), 26118-26125.

21. Yang, Q.; Zhou, J.; Zhang, G.; Guo, C.; Li, M.; Zhu, Y.; Qian, Y., Sb nanoparticles uniformly dispersed in 1-D N-doped porous carbon as anodes for Li-ion and Na-ion batteries. *Journal of Materials Chemistry A* **2017**, *5* (24), 12144-12148.

22. Farbod, B.; Cui, K.; Kalisvaart, W. P.; Kupsta, M.; Zahiri, B.; Kohandehghan, A.; Lotfabad, E. M.; Li, Z.; Lubner, E. J.; Mitlin, D., Anodes for sodium ion batteries based on tin-germanium-antimony alloys. *ACS nano* **2014**, *8* (5), 4415-4429.

23. Liu, J.; Yang, Z.; Wang, J.; Gu, L.; Maier, J.; Yu, Y., Three-dimensionally interconnected nickel-antimony intermetallic hollow nanospheres as anode material for high-rate sodium-ion batteries. *Nano Energy* **2015**, *16*, 389-398.

24. Lu, Y.; Zhang, N.; Jiang, S.; Zhang, Y.; Zhou, M.; Tao, Z.; Archer, L. A.; Chen, J., High-Capacity and Ultrafast Na-Ion Storage of a Self-Supported 3D Porous Antimony Persulfide-Graphene Foam Architecture. *Nano Lett* **2017**, *17* (6), 3668-3674.

25. Kwon, T. W.; Choi, J. W.; Coskun, A., The emerging era of supramolecular polymeric binders in silicon anodes. *Chem Soc Rev* **2018**, *47* (6), 2145-2164.

26. Kovalenko, I.; Zdyrko, B.; Magasinski, A.; Hertzberg, B.; Milicev, Z.; Burtovyy, R.; Luzinov, I.; Yushin, G., A major constituent of brown algae for use in high-capacity Li-ion batteries. *Science* **2011**, *334* (6052), 75-9.

27. Lee, J.-H.; Lee, S.; Paik, U.; Choi, Y.-M., Aqueous processing of natural graphite particulates for lithium-ion battery anodes and their electrochemical performance. *Journal of Power Sources* **2005**, *147* (1-2), 249-255.

28. Murase, M.; Yabuuchi, N.; Han, Z. J.; Son, J. Y.; Cui, Y. T.; Oji, H.; Komaba, S., Crop-derived polysaccharides as binders for high-capacity silicon/graphite-based electrodes in lithium-ion batteries. *ChemSusChem* **2012**, *5* (12), 2307-11.

29. Magasinski, A.; Zdyrko, B.; Kovalenko, I.; Hertzberg, B.; Burtovyy, R.; Huebner, C. F.; Fuller, T. F.; Luzinov, I.; Yushin, G., Toward efficient binders for Li-ion battery Si-based anodes: polyacrylic acid. *ACS Appl Mater Interfaces* **2010**, *2* (11), 3004-10.

30. Liu, J.; Zhang, Q.; Zhang, T.; Li, J.-T.; Huang, L.; Sun, S.-G., A Robust Ion-Conductive Biopolymer as a Binder for Si Anodes of Lithium-Ion Batteries. *Advanced Functional Materials* **2015**, *25* (23), 3599-3605.

31. Kwon, T. W.; Jeong, Y. K.; Lee, I.; Kim, T. S.; Choi, J. W.; Coskun, A., Systematic molecular-level design of binders incorporating Meldrum's acid for silicon anodes in lithium rechargeable batteries. *Adv Mater* **2014**, *26* (47), 7979-85.

32. Koo, B.; Kim, H.; Cho, Y.; Lee, K. T.; Choi, N. S.; Cho, J., A highly cross-linked polymeric binder for high-performance silicon negative electrodes in lithium ion batteries. *Angew Chem Int Ed Engl* **2012**, *51* (35), 8762-7.

33. Balzer, B. N.; Gallei, M.; Hauf, M. V.; Stallhofer, M.; Wiegler, L.;

Holleitner, A.; Rehahn, M.; Hugel, T., Nanoscale friction mechanisms at solid-liquid interfaces. *Angew Chem Int Ed Engl* **2013**, *52* (25), 6541-4.

34. Kienle, S.; Gallei, M.; Yu, H.; Zhang, B.; Krysiak, S.; Balzer, B. N.; Rehahn, M.; Schluter, A. D.; Hugel, T., Effect of molecular architecture on single polymer adhesion. *Langmuir* **2014**, *30* (15), 4351-7.

35. Yabuuchi, N.; Kubota, K.; Dahbi, M.; Komaba, S., Research development on sodium-ion batteries. *Chem Rev* **2014**, *114* (23), 11636-82.

36. Wen, Y.; He, K.; Zhu, Y.; Han, F.; Xu, Y.; Matsuda, I.; Ishii, Y.; Cumings, J.; Wang, C., Expanded graphite as superior anode for sodium-ion batteries. *Nat Commun* **2014**, *5*, 4033.

37. Wang, J. W.; Liu, X. H.; Mao, S. X.; Huang, J. Y., Microstructural evolution of tin nanoparticles during in situ sodium insertion and extraction. *Nano letters* **2012**, *12* (11), 5897-5902.

38. Darwiche, A.; Marino, C.; Sougrati, M. T.; Fraise, B.; Stievano, L.; Monconduit, L., Correction to "Better Cycling Performances of Bulk Sb in Na-Ion Batteries Compared to Li-Ion Systems: An Unexpected Electrochemical Mechanism". *Journal of the American Chemical Society* **2013**, *135* (27), 10179-10179.

39. He, M.; Kravchyk, K.; Walter, M.; Kovalenko, M. V., Monodisperse antimony nanocrystals for high-rate Li-ion and Na-ion battery anodes: nano versus bulk. *Nano Lett* **2014**, *14* (3), 1255-62.

40. Li, J.; Lewis, R.; Dahn, J., Sodium carboxymethyl cellulose a potential binder for Si negative electrodes for Li-ion batteries. *Electrochemical and Solid-State Letters* **2007**, *10* (2), A17-A20.

41. Gao, H.; Zhou, W.; Jang, J.-H.; Goodenough, J. B., Cross-Linked Chitosan as a Polymer Network Binder for an Antimony Anode in Sodium-Ion Batteries. *Advanced Energy Materials* **2016**, *6* (6).

42. Hong, S. Y.; Kim, Y.; Park, Y.; Choi, A.; Choi, N.-S.; Lee, K. T., Charge carriers in rechargeable batteries: Na ions vs. Li ions. *Energy & Environmental Science* **2013**, *6* (7).

43. Kim, H.; Kim, H.; Ding, Z.; Lee, M. H.; Lim, K.; Yoon, G.; Kang, K., Recent Progress in Electrode Materials for Sodium-Ion Batteries. *Advanced Energy Materials* **2016**, *6* (19).

44. Dai, K.; Zhao, H.; Wang, Z.; Song, X.; Battaglia, V.; Liu, G., Toward high specific capacity and high cycling stability of pure tin nanoparticles with conductive polymer binder for sodium ion batteries. *Journal of Power Sources* **2014**, *263*, 276-279.

45. Kim, Y.-S.; Cho, Y.-G.; Odkhuu, D.; Park, N.; Song, H.-K., A physical organogel electrolyte: characterized by in situ thermo-irreversible gelation and single-ion-predominant conduction. *Scientific reports* **2013**, *3*, 1917.

46. Linarez Pérez, O. E.; Sánchez, M. D.; López Teijelo, M., Characterization of growth of anodic antimony oxide films by ellipsometry and XPS. *Journal of Electroanalytical Chemistry* **2010**, *645* (2), 143-148.

47. Karkar, Z.; Guyomard, D.; Roué, L.; Lestriez, B., A comparative study of polyacrylic acid (PAA) and carboxymethyl cellulose (CMC) binders for Si-based electrodes. *Electrochimica Acta* **2017**, *258*, 453-466.

48. Li, C.; Liu, X., Mechanical and thermal properties study of glass fiber reinforced polyarylene ether nitriles. *J Materials Letters* **2007**, *61* (11-12), 2239-2242.

49. Marszalek, P. E.; Oberhauser, A. F.; Pang, Y.-P.; Fernandez, J. M., Polysaccharide elasticity governed by chair-boat transitions of the glucopyranose ring. *Nature* **1998**, *396*

(6712), 661.

50. McLaren, A., Adhesion of high polymers to cellulose. Influence of structure, polarity, and tack temperature. *Journal of polymer science* **1948**, 3 (5), 652-662.
51. Sivaramakrishnan, K.; Marvel, C., Aromatic polyethers, polysulfones, and polyketones as laminating resins. II. *Journal of Polymer Science: Polymer Chemistry Edition* **1974**, 12 (3), 651-662.
52. Alia, J.; Edwards, H.; Moore, J., Fourier transform Raman spectroscopic study of lithium perchlorate solutions in acrylonitrile. *Journal of Raman Spectroscopy* **1995**, 26 (8-9), 715-726.
53. Croce, F.; Brown, S. D.; Greenbaum, S. G.; Slane, S. M.; Salomon, M., Lithium-7 NMR and ionic conductivity studies of gel electrolytes based on polyacrylonitrile. *Chemistry of materials* **1993**, 5 (9), 1268-1272.
54. Huang, B.; Wang, Z.; Chen, L.; Xue, R.; Wang, F., The mechanism of lithium ion transport in polyacrylonitrile-based polymer electrolytes. *Solid State Ionics* **1996**, 91 (3-4), 279-284.
55. Pignanelli, F.; Romero, M.; Faccio, R.; Mombro, A. W., Experimental and Theoretical Study of Ionic Pair Dissociation in a Lithium Ion-Linear Polyethylenimine-Polyacrylonitrile Blend for Solid Polymer Electrolytes. *J Phys Chem B* **2017**, 121 (27), 6759-6765.
56. Shen, Y.; Deng, G. H.; Ge, C.; Tian, Y.; Wu, G.; Yang, X.; Zheng, J.; Yuan, K., Solvation structure around the Li(+) ion in succinonitrile-lithium salt plastic crystalline electrolytes. *Phys Chem Chem Phys* **2016**, 18 (22), 14867-73.
57. Takada, K.; Yamada, Y.; Watanabe, E.; Wang, J.; Sodeyama, K.; Tateyama, Y.; Hirata, K.; Kawase, T.; Yamada, A., Unusual Passivation Ability of Superconcentrated Electrolytes toward Hard Carbon Negative Electrodes in Sodium-Ion Batteries. *ACS Appl Mater Interfaces* **2017**, 9 (39), 33802-33809.
58. Taniguchi, M.; Kawai, T., Vertical electrochemical transistor based on poly(3-hexylthiophene) and cyanoethylpullulan. *Applied Physics Letters* **2004**, 85 (15), 3298-3300.
59. Xu, W.; Rhee, S.-W., Low-operating voltage organic field-effect transistors with high-k cross-linked cyanoethylated pullulan polymer gate dielectrics. *Journal of Materials Chemistry* **2009**, 19 (29).
60. Shibuya, N., Kainuma, Keiji Dielectric relaxation in solid dextran and pullulan. *Die Makromolekulare Chemie: Macromolecular Chemistry* **1985**, 186 (2), 433-438.
61. Hou, H.; Jing, M.; Yang, Y.; Zhang, Y.; Zhu, Y.; Song, W.; Yang, X.; Ji, X., Sb porous hollow microspheres as advanced anode materials for sodium-ion batteries. *Journal of Materials Chemistry A* **2015**, 3 (6), 2971-2977.
62. Liang, L.; Xu, Y.; Wang, C.; Wen, L.; Fang, Y.; Mi, Y.; Zhou, M.; Zhao, H.; Lei, Y., Large-scale highly ordered Sb nanorod array anodes with high capacity and rate capability for sodium-ion batteries. *Energy & Environmental Science* **2015**, 8 (10), 2954-2962.
63. Darwiche, A.; Marino, C.; Sougrati, M. T.; Fraise, B.; Stievano, L.; Monconduit, L., Better cycling performances of bulk Sb in Na-ion batteries compared to Li-ion systems: an unexpected electrochemical mechanism. *J Am Chem Soc* **2012**, 134 (51), 20805-11.
64. Zhu, Y.; Han, X.; Xu, Y.; Liu, Y.; Zheng, S.; Xu, K.; Hu, L.; Wang, C., Electrospun Sb/C fibers for a stable and fast sodium-ion battery anode. *ACS nano* **2013**, 7 (7), 6378-6386.
65. Qian, J.; Chen, Y.; Wu, L.; Cao, Y.; Ai, X.; Yang, H., High capacity Na-

storage and superior cyclability of nanocomposite Sb/C anode for Na-ion batteries. *Chemical Communications* **2012**, 48 (56), 7070-7072.

66. Wu, L.; Hu, X.; Qian, J.; Pei, F.; Wu, F.; Mao, R.; Ai, X.; Yang, H.; Cao, Y., Sb–C nanofibers with long cycle life as an anode material for high-performance sodium-ion batteries. *Energy & Environmental Science* **2014**, 7 (1), 323-328.

67. Fan, L.; Zhang, J.; Cui, J.; Zhu, Y.; Liang, J.; Wang, L.; Qian, Y., Electrochemical performance of rod-like Sb–C composite as anodes for Li-ion and Na-ion batteries. *Journal of Materials Chemistry A* **2015**, 3 (7), 3276-3280.

68. Zhao, X.; Vail, S. A.; Lu, Y.; Song, J.; Pan, W.; Evans, D. R.; Lee, J.-J.; interfaces, Antimony/graphitic carbon composite anode for high-performance sodium-ion batteries. *ACS applied materials & interfaces* **2016**, 8 (22), 13871-13878.

69. Zhang, N.; Liu, Y.; Lu, Y.; Han, X.; Cheng, F.; Chen, J., Spherical nano-Sb@C composite as a high-rate and ultra-stable anode material for sodium-ion batteries. *Nano Research* **2015**, 8 (10), 3384-3393.

70. Chan, C. K.; Ruffo, R.; Hong, S. S.; Cui, Y., Surface chemistry and morphology of the solid electrolyte interphase on silicon nanowire lithium-ion battery anodes. *Journal of Power Sources* **2009**, 189 (2), 1132-1140.

71. Jang, J. Y.; Lee, Y.; Kim, Y.; Lee, J.; Lee, S.-M.; Lee, K. T.; Choi, N.-S., Interfacial architectures based on a binary additive combination for high-performance Sn 4 P 3 anodes in sodium-ion batteries. *Journal of Materials Chemistry A* **2015**, 3 (16), 8332-8338.

72. Leroy, S.; Blanchard, F.; Dedryvère, R.; Martinez, H.; Carré, B.; Lemordant, D.; Gonbeau, D., Surface film formation on a graphite electrode in Li-ion batteries: AFM and XPS study. *Surface and Interface Analysis* **2005**, 37 (10), 773-781.

73. Darwiche, A.; Bodenes, L.; Madec, L.; Monconduit, L.; Martinez, H., Impact of the salts and solvents on the SEI formation in Sb/Na batteries: An XPS analysis. *Electrochimica Acta* **2016**, 207, 284-292.

74. Dedryvère, R.; Gireaud, L.; Grugeon, S.; Laruelle, S.; Tarascon, J.-M.; Gonbeau, D., Characterization of lithium alkyl carbonates by X-ray photoelectron spectroscopy: experimental and theoretical study. *The Journal of Physical Chemistry B* **2005**, 109 (33), 15868-15875.